Atmos. Meas. Tech. Discuss., 7, 10619–10671, 2014
www.atmos-meas-tech-discuss.net/7/10619/2014/
doi:10.5194/amtd-7-10619-2014

Atmospheric Measurement Techniques Discussions
Open Access

Improved spectral fitting of nitrogen dioxide from OMI in the 405–465 nm window

J. H. G. M. van Geffen[1], K. F. Boersma[1,2], M. Van Roozendael[3], F. Hendrick[3], E. Mahieu[4], I. De Smedt[3], M. Sneep[1], and J. P. Veefkind[1,5]

[1]Royal Netherlands Meteorological Institute (KNMI), De Bilt, the Netherlands
[2]Wageningen University (WUR), Wageningen, the Netherlands
[3]Belgium Institute for Space Aeronomy (BIRA-IASB), Brussels, Belgium
[4]University of Liège (ULg), Liège, Belgium
[5]Delft University of Technology (TUDelft), Delft, the Netherlands

Received: 16 June 2014 – Accepted: 29 September 2014 – Published: 21 October 2014

Correspondence to: J. H. G. M. van Geffen (geffen@knmi.nl)

Published by Copernicus Publications on behalf of the European Geosciences Union.

Abstract

An improved nitrogen dioxide (NO_2) slant column density retrieval for the Ozone Monitoring Instrument (OMI) in the 405–465 nm spectral region is presented. Since the launch of OMI on board NASA's EOS-Aura satellite in 2004, DOAS retrievals of NO_2 slant column densities have been the starting point for the KNMI DOMINO (v2.0) and NASA SP (v2.1) retrievals. However, recent intercomparisons between NO_2 retrievals from OMI and other UV/Vis and limb spectrometers, as well as ground-based measurements, clearly suggested that OMI stratospheric NO_2 is biased high.

This study revises the OMI NO_2 retrieval in detail. The representation of the OMI slit function to convolve high-resolution reference spectra onto the relevant spectral grid is improved. The window used for the wavelength calibration is optimised, leading to much-reduced fitting errors. Ozone and water vapour spectra used in the fit are updated, reflecting the recently improved knowledge on their absorption cross section as documented in the literature. The improved spectral fit also accounts for absorption by the O_2–O_2 collision complex and by liquid water over clear-water areas.

The main changes in the improved spectral fitting result from the updates related to the wavelength calibration: the RMS error of the fit is reduced by 23 % and the NO_2 slant column by 0.85×10^{15} molec cm^{-2}, independent of latitude, solar zenith angle and NO_2 value. Including O_2–O_2 and liquid water absorption and updating the O_3 and water vapour cross-section spectra further reduces NO_2 slant columns on average by 0.35×10^{15} molec cm^{-2}, accompanied with a further 9 % reduction in the RMS error of the fit.

The improved OMI NO_2 slant columns are consistent with independent NO_2 retrievals to within a range that can be explained by photo-chemically driven diurnal increases in stratospheric NO_2 and by small differences in fitting window and fitting approach. The revisions indicate that current OMI NO_2 slant columns suffered mostly from an additive, positive offset that is removed by the improved wavelength calibration and representation of the OMI slit function. It is therefore anticipated that the improved

AMTD

7, 10619–10671, 2014

NO_2 slant columns are most important to retrievals of spatially homogeneous stratospheric NO_2 rather than to heterogeneous tropospheric NO_2.

1 Introduction

Nitrogen dioxide (NO_2) and nitrogen oxide (NO) – together usually referred to as nitrogen oxides (NO_x = NO + NO_2) – are important trace gases in the Earth's atmosphere. They enter the atmosphere due to anthropogenic (e.g. fossil fuel combustion, biomass burning) and natural (e.g. microbiological processes in soils, wild fires, lightning) processes. Approximately 95 % of the NO_x emissions is in the form of NO. In the presence of sunlight, a photochemical cycle involving ozone (O_3) converts NO into NO_2 and vice versa on a timescale of minutes, making NO_2 a robust measure for concentrations of NO_x (e.g. Jacob, 1999). Over remote regions the NO_2 is primarily located in the stratosphere (typically more than 90 %). For polluted regions 50–90 % of the total NO_2 column is located in the troposphere, depending on the degree of pollution, with most of the tropospheric NO_2 in the planetary boundary layer. Vertically integrated NO_2 concentrations are $1–2 \times 10^{15}$ molec cm^{-2} in the stratosphere, and up to 10 times more in the troposphere over polluted areas. For typical levels of OH the lifetime of NO_x in the lower troposphere is less than a day (e.g. Schaub et al., 2007; Beirle et al., 2011).

Boundary layer NO_2 directly affects human health (WHO, 2003). In addition nitrogen oxides are essential precursors for the photochemical formation of ozone (Sillman et al., 1990), they influence concentrations of OH and thereby influence the lifetime of methane (Fuglestvedt et al., 1999) and other gases. NO_2 in itself is a minor greenhouse gas, but the indirect effects of NO_2 on global climate change are probably larger, with a presumed net cooling effect mostly driven by oxidation-fueled aerosol formation (Shindell et al., 2009). Stratospheric NO_2 originates mainly from oxidation of N_2O in the middle stratosphere, which leads to NO_x, which in turn acts as a catalyst for ozone destruction (Crutzen, 1970; Hendrick et al., 2012). Stratospheric NO_x can also suppress

AMTD
7, 10619–10671, 2014

ozone depletion by converting reactive chlorine and hydrogen compounds into unreactive reservoir species (such as $ClONO_2$ and HNO_3; Murphy et al., 1993).

The important role of NO_2 in both troposphere and stratosphere requires monitoring of its concentration distribution on a global scale. Observations from satellite instruments provide global coverage complementary to sparse measurements by ground-based and in-situ (balloon, aircraft) instruments. NO_2 column densities have been retrieved using the Differential Optical Absorption Spectroscopy (DOAS) technique from space since the mid-90s from data aquired by the nadir-viewing UV/Vis backscatter instruments GOME (Burrows et al., 1999), SCIAMACHY (Bovensmann et al., 1999), OMI (Levelt et al., 2006), and the GOME-2 instruments (Munro et al., 2006) aboard MetOp-A and MetOp-B. TROPOMI (Veefkind et al., 2012), scheduled for launch in 2016, will extend the record of these observations.

The retrieval of NO_2 from satellite measured spectra with DOAS is well-possible, but not easy: the structure of the NO_2 differential absorption is weak and there are interfering signals from the surface, the atmosphere and instrumental issues. Most retrievals of NO_2 concentrations are performed in the visible range between 400 and 500 nm. These retrievals need to take into account the absorption by other trace gases relevant in this wavelength range, in particular ozone, water vapour, the O_2–O_2 collision complex, and liquid water. Over tropical forests, detectable contributions from glyoxal (CHOCHO) have been reported (e.g. Lerot et al., 2010). In addition, Rotational Raman Scattering (the so-called "Ring effect"; see Grainger and Ring, 1962; Chance and Spurr, 1997), plays an imporant role.

This paper describes a revision of NO_2 slant column retrieval from level-1b spectra measured by OMI since 2004. The study was prompted by the observation, reported first by N. Krotkov at the EOS-Aura meeting in October 2012 (Krotkov et al., 2012), that OMI stratospheric NO_2 concentrations are systematically higher than those derived from SCIAMACHY and GOME-2 measurements by $0.5–1 \times 10^{15}$ molec cm^{-2}, after accounting for the daytime increase in stratospheric NO_2 (Dirksen et al., 2011). Recently, Belmonte-Rivas et al. (2014) confirmed the high bias in OMI stratospheric columns,

Discussion Paper | Discussion Paper | Discussion Paper | Discussion Paper |
AMTD
7, 10619–10671, 2014
Improved spectral fitting of nitrogen dioxide from OMI
J. H. G. M. van Geffen et al.

compared to an ensemble of stratospheric NO_2 retrievals from limb-sounding sensors. The revision is further motivated by recent updates to relevant absorption cross section spectra, the inclusion of previously neglected absorption signatures from liquid water absorption (Richter et al., 2011; Lerot et al., 2010), and the modification of the OMI level-1b spectra following the first appearance of the so-called row anomaly in 2007, but not yet evaluated for its effects on the DOAS NO_2 retrieval.

2 Observations of NO_2 column densities

2.1 UV-Vis satellite based observations

2.1.1 The satellite based instruments

OMI (Levelt et al., 2006) is a spectrometer aboard the EOS-Aura satellite and operates since 2004. The instrument measures backscattered and direct sunlight in the UV and visible (270–500 mm) from a sun-synchronous orbit. The spectral resolution and spectral sampling in the visible wavelength range are 0.63 and 0.21 nm, respectively. The overpass is at about 13:40 local time (LT), with the satellite flying south-to-north on the dayside of the Earth. Individual nadir ground pixels are 13 by 24 km^2 at the middle of the swath; the size of the pixels increases towards the edges of the swath. The full swath width is about 2600 km and OMI achieves global coverage each day.

The first GOME-2 instrument (Munro et al., 2006) is a spectrometer aboard the MetOp-A satellite and operates since 2007. The instrument measures backscattered and direct sunlight in the UV, visible and near-infrared (220–790 nm) from a sun-synchronous orbit. The spectral resolution and spectral sampling in the visible wavelength range are 0.51 and 0.21 nm, respectively. The overpass is at about 09:30 LT, with the satellite flying north-to-south on the dayside of the Earth. Individual nadir ground pixels are 40 by 80 km^2. The full swath width is about 1920 km and with that GOME-2 achieves nearly global coverage each day. A second, identical GOME-2 instrument

AMTD
7, 10619–10671, 2014

was launched aboard the MetOp-B satellite in 2012. In this paper GOME-2 refers to the instrument aboard MetOp-A, sometimes referred to as GOME-2A.

SCIAMACHY (Bovensmann et al., 1999) is a spectrometer aboard the satellite ENVISAT and operated in the period 2002–2012. The instrument measured backscattered and direct sunlight in the UV, visible and near-infrared (220–2380 nm) from a sun-synchronous orbit. The spectral resolution and spectral sampling in the visible wavelength range are 0.44 and 0.2 nm, respectively. The overpass was at about 10:00 LT, with the satellite flying north-to-south on the dayside of the Earth. Individual nadir ground pixels were 30 by 60 km^2. The full swath width was about 960 km. Since SCIAMACHY measured alternatively in a nadir and limb viewing mode, it achieved global coverage once every 6 days.

2.1.2 NO_2 spectral fitting

The Differential Optical Absorption Spectroscopy (DOAS; Platt, 1994; Platt and Stutz, 2008) technique is applied to the backscattered spectra measured by the satellite instrument to obtain the NO_2 slant column density (SCD). The SCD is the integrated concentration of NO_2 over light paths from the Sun through the Earth's atmosphere to the satellite, weighted with their relative contribution to the radiance. The DOAS retrieval technique is described in Sect. 2.2.

The OMI NO_2 SCD data are calculated at NASA by a processor named OMNO2A. The retrieval results of OMNO2A are input for subsequent processing to determine NO_2 vertical column densities (VCDs), e.g. for the DOMINO data product of KNMI (e.g. Boersma et al., 2002, 2011; Dirksen et al., 2011) and NASA's NO_2 Standard Product (SP; e.g. Bucsela et al., 2006, 2013). For the OMI NO_2 retrieval, the selected spectral fitting window is 405–465 nm, wider than the often used 425–450 nm window in order to improve the effective signal-to-noise. The degree of the DOAS polynomial is 5, higher than for other retrievals in view of the wider retrieval window.

For GOME-2 and SCIAMACHY NO_2 SCD data, BIRA-IASB uses a processor based on QDOAS (Danckaert et al., 2012), the multi-platform successor of their WinDOAS

AMTD
7, 10619–10671, 2014

package; see e.g. Van Roozendael et al. (2006) and Lerot et al. (2009). The DOAS fit on GOME-2 and SCIAMACHY data use almost the same wavelength window: 425.0–450.0 and 426.5–451.5 nm, respectively (the small difference between the fit windows is related to instrumental issues). The degree of the DOAS polynomial is 3 for GOME-2 and 2 for SCIAMACHY.

Table 1 provides an overview of the details of the DOAS retrieval for the OMI, GOME-2 and SCIAMACHY sensors used in this study.

2.2 DOAS retrieval of NO_2 slant column densities

In the DOAS technique, an analytical function that describes the relevant atmospheric physical processes (scattering, reflection and absorption) is matched to the satellite-measured spectrum. The analytical function or physical model contains a low-order polynomial that represents the spectrally smooth part of the spectrum, related to slowly varying broad-band absorption as well as Rayleigh and Mie scattering processes in the atmosphere and smooth surface reflection and absorption effects.

The physical model furthermore includes a number of terms that represent the spectrally varying absorption signatures of relevant absorbers in the spectral window, notably NO_2, ozone (O_3) and water vapour (H_2O_{vap}). In the SCIAMACHY and GOME-2 NO_2 retrievals also absorption by O_2–O_2 is taken into account, while for OMNO2A this is currently not done (see Table 1). In addition, the physical model accounts for inelastic scattering that leads to filling-in of the Fraunhofer lines in the radiance spectrum, the so-called "Ring effect", by describing these effects as a pseudo-absorber, that is by including a Ring reference absorption spectrum along with the molecular absorption terms.

The DOAS procedure minimises the difference between the measured spectrum $R_{meas}(\lambda)$ and a modelled spectrum $R_{mod}(\lambda)$ within a given wavelength window, in the form of minimisation of a chi-squared merit function. The measured reflectance $R_{meas}(\lambda)$ is determined from the radiance measured at top-of-atmosphere $I(\lambda)$ and the extraterrestrial solar irradiance spectrum $I_0(\lambda)$.

In the OMI slant column retrieval the modelled reflectance is expressed in terms of intensities, which leads to a non-linear fit problem and allows to describe the effects of inelastic scattering after a scattering event has occured:

$$R_{\text{mod}}(\lambda) = P(\lambda) \cdot \exp\left[- \sum_{k=1}^{N_k} \sigma_k(\lambda) \cdot N_{\text{s},k} \right] \cdot \left(1 + C_{\text{ring}} \frac{I_{\text{ring}}(\lambda)}{I_0(\lambda)} \right) \tag{1}$$

with $P(\lambda)$ a polynomial of degree N_p, $\sigma_k(\lambda)$ the cross section and $N_{\text{s},k}$ the slant column amount of molecule k taken into account in the fit (NO_2, O_3, etc.), C_{ring} the Ring fitting coefficient and $I_{\text{ring}}(\lambda)/I_0(\lambda)$ the sun-normalised synthetic Ring spectrum. The Ring spectrum describes the differential spectral signatures arising from inelastic Raman scattering of incoming sunlight by N_2 and O_2 molecules. The last term between brackets in Eq. (1) describes both the contribution of the direct differential absorption (i.e. the 1), and the modification of these differential structures by inelastic scattering (the $+C_{\text{ring}} I_{\text{ring}}(\lambda)/I_0(\lambda)$ term) to the reflectance spectrum. Some further details on the OMI NO_2 DOAS slant column retrieval can be found in the Supplement, Sect. S1.

2.3 Ground-based observations in UV-Vis and IR

Satellite observations of NO_2 have been compared to ground-based measurements in several studies. Hendrick et al. (2012), for example, performed an extensive comparison of measurements acquired at the Jungfraujoch station (46.5° N, 8.0° E), part of NDACC (Network for the Detection of Atmospheric Composition Change), with data from GOME-2 and SCIAMACHY. The Jungfraujoch station is located at 3580 m a.s.l., which means that most of the year the observatory is above the boundary layer and the instruments measure NO_2 in the free troposphere and stratosphere. Hendrick et al. (2012) found that the data of independent SAOZ and FTIR measurements match each other and stratospheric NO_2 data from GOME-2 and SCIAMACHY quite well (with SAOZ biased by +8 % w.r.t. FTIR).

The SAOZ instrument, operated by BIRA-IASB, is a broad-band (300–600 nm) spectrometer that measures zenith scattered sunlight (Pommereau end Goutail, 1988). Vertical column densities are derived by using the standard four-step approach (e.g. Hendrick et al., 2012), using the NDACC UV/Vis Working Group recommendations. Since these are described in detail on the NDACC website[1], only the main features are given here. The NO_2 is retrieved in the 425–495 nm wavelength window, taking into account absorption by NO_2, ozone, water vapour and O_2–O_2, the Ring effect, and a 3rd order polynomial. In the conversion of slant to vertical NO_2 columns, the NDACC NO_2 AMF climatology based on the harmonic climatology of stratospheric NO_2 profile developed by Lambert et al. (1999, 2000) has been used. SAOZ measurements contaminated by strong pollution events coming from the valley below the station have been filtered out.

Using the BIRA-IASB stacked box photochemical model PSCBOX (Hendrick et al., 2004), daily initialized with SLIMCAT chemical and meteorological fields, a photochemical correction is determined: for each day, 90° SZA sunrise and sunset SAOZ data are converted to the satellite overpass SZA of that day, after which the average of both SAOZ NO_2 column values can be compared to the corresponding satellite measurement.

The FTIR instrument, operated by the University of Liège, is a spectrometer that measures high-resolution solar absorption spectra under clear-sky conditions (Zander et al., 2008). The NO_2 retrieval is extensively described by Hendrick et al. (2012). In brief, two microwindows are used: 2914.6–2914.7 and 2915.0–2915.11 cm^{-1}, taking into account absorption by ozone, water vapour and methane. Vertical profiles and corresponding column densities are derived using the Optimal Estimation-based SFIT-2 algorithm (e.g. Rinsland et al., 1998). Here also, a photochemical correction determined with the PSCBOX model is applied to the column data: for each day where FTIR measurements are available, all retrieved FTIR vertical columns are photochemically converted to the satellite overpass SZA of that day, after which the average of

[1]See on http://wwww.ndacc.org/ the UV/Vis (@BIRA) page.

AMTD

7, 10619–10671, 2014

all corrected FTIR NO_2 columns of the day is compared to the corresponding satellite measurement.

Total random and systematic uncertainties on the FTIR column data have been evaluated at 11 and 36 %, respectively (Hendrick et al., 2012; Table 2 in Rinsland et al., 2003). In the case of SAOZ measurements, error sources have been quoted in Van Roozendael et al. (1994) and Hendrick et al. (2012). Taking into account the past NDACC NO_2 intercomparison exercises (e.g. Vandaele et al., 2005; Roscoe et al., 2010), a total uncertainty of 12 % on the retrieved NO_2 vertical columns is derived.

3 Intercomparisons of statrospheric NO_2 columns

3.1 Comparison of satellite retrieval results

NO_2 data from OMI, GOME-2 and SCIAMACHY are evaluated for 2007, a year for which data is available and of good quality for all instruments. Stratospheric NO_2 concentrations are best detected over the Pacific Ocean, where tropospheric contributions to the NO_2 column are small in the absence of substantial sources of pollution. Satellite data is compared for the the Pacific Ocean area, defined here as the area from 60° S to 60° N and from 140 to 180° W. DOMINO v2.0 data is used for OMI (Boersma et al., 2011), TM4NO2A v2.1 for GOME-2 and TM4NO2A v2.0 for SCIAMACHY (Boersma et al., 2004).

Figure 1 shows the monthly average stratospheric NO_2 column for the three instruments and their mutual differences as function of latitude for March 2007 (top panel) and September 2007 (bottom panel). The OMI stratospheric columns are clearly higher than those of GOME-2 by about 1.0×10^{15} molec cm^{-2}. The GOME-2 stratospheric columns in turn are higher than SCIAMACHY's by 0.1–0.3 $\times 10^{15}$ molec cm^{-2}. These findings are consistent with those from Belmonte-Rivas et al. (2014), who reported a similar high bias in OMI and low bias in SCIAMACHY data relative to stratospheric NO_2 columns obtained from an ensemble of limb and nadir sensors.

To illustrate the uncertainties in the stratospheric NO_2 column an error bar is plotted near the equator in Fig. 1 for the three instruments, which represents the average over the standard deviations of the stratospheric columns for that latitude bin. Since most NO_2 over the Pacific Ocean is stratospheric, the standard deviation of the stratospheric VCD is estimated from the standard deviation of the total VCD for all three instruments.

Figure 1 shows that there is only a weak variability of the intra-sensor differences with latitude and that the differences are similar to within 0.2×10^{15} molec cm^{-2}; for the other months of 2007 (not shown) the results are quite similar. This weak variability with latitude and independence of the month indicates that the differences between the instruments is dominated by an additive offset.

Table 2 lists the annual averages of the intra-sensor differences over the Pacific Ocean area for 2007. The difference of 1.1–1.3 $\times 10^{15}$ molec cm^{-2} between OMI (overpass at 13:40 LT) and the two mid-morning sensor is considerably larger than the increase of stratospheric NO_2 between the respective measurement times. Photochemical models suggest a latitude-dependent increase of 10–30 % in stratospheric NO_2 between 09:30 and 13:40 LT. This increase reflects the production of NO_2 from N_2O_5 photodissociation and corresponds to an increase of 0.1–0.6 $\times 10^{15}$ molec cm^{-2} (Dirksen et al., 2011; Belmonte-Rivas et al., 2014).

3.2 Comparison with ground-based NO_2 data

The comparison of SAOZ and FTIR data at the Jungfraujoch station with satellite data by Hendrick et al. (2012) (cf. Sect. 2.3) was repeated now also including OMI data and extending the GOME-2 and SCIAMACHY datasets up to the end of 2012. For this comparison the SAOZ and FTIR data have been corrected with a photochemical model (PSCBOX; Hendrick et al., 2004) to the local overpass times of the satellite sensors. For the Jungfraujoch station the model predicts an average temporal difference between OMI and the mid-morning sensors GOME-2 and SCIAMACHY of $+0.5 \times 10^{15}$ molec cm^{-2}.

AMTD
7, 10619–10671, 2014

J. H. G. M. van Geffen et al.

Figure 2 shows the averaged monthly mean differences between the three satellite sensors and the SAOZ and FTIR measurements for 2007–2012. Since the data of GOME-2, SCIAMACHY, SAOZ and FTIR agree to within 0.2×10^{15} molec cm^{-2}, the ground-based measurements clearly suggest that OMI stratospheric NO_2 retrievals are biased high by $0.3–0.8 \times 10^{15}$ molec cm^{-2}, or $+0.5 \times 10^{15}$ molec cm^{-2} on average. Table 3 provides an overview of the yearly mean differences over the 2007–2012 period, as well as for the complete sensor records of SCIAMACHY (2002–2012) and OMI (2004–2012). The difference between the GOME-2 and SCIAMACHY results is of the order of 0.1×10^{15} molec cm^{-2}, which is consistent with the offset between GOME-2 and SCIAMACHY in stratospheric NO_2 over the Pacific Ocean.

3.3 Origin of the OMI stratospheric NO_2 bias

The results of the comparisons discussed above suggest strongly that OMI stratospheric NO_2 is biased high. Since the air-mass factor calculations for NO_2 in the stratosphere are straightforward (with an error of less than 1 %), the high bias in OMI stratospheric columns originates from the slant column retrieval. As a result of this finding, the details of the OMI NO_2 spectral fitting OMNO2A were revisited, which has resulted in the improvements described in the next section.

4 Improvements to the OMI NO_2 retrieval

4.1 Reference spectra

The set of reference spectra used in the spectral fit of the current OMNO2A processing have been introduced in August 2006, with a reprocessing of the available OMI data record. Since then a number of improved reference spectra datasets have been reported in the peer-reviewed literature. In addition, the reference spectra used in the current OMNO2A processing have been convolved with the OMI slit function measured during the on-ground calibration, described by a parametrised broadened Gaussian function (Dirksen et al., 2006), but without taking the wavelength and row dependency of the slit function into account.

For these reasons all relevant cross sections are generated anew, based on the latest established absorption spectra, and convolved with the OMI slit function, but now taking the wavelength and row dependency of the slit function into account in the form of a row-average slit function. Details of the OMI slit function[2] and the implementation of the convolution are given in Sect. S2 of the Supplement. All convolved reference spectra thus created are given a 0.01 nm sampling.

Figure 3 shows the updated reference spectra taken into account in the forthcoming OMNO2A slant column reprocessing: the NO_2, O_3, water vapour (H_2O_{vap}), O_2–O_2 and liquid water (H_2O_{liq}) cross sections and the Ring radiance spectrum $I_{ring}(\lambda)$. The reference spectra labelled hereafter "v2006" refer to those used in the current OMNO2A processor (used in e.g. the DOMINO v2.0 dataset), while "v2014" refers to the updated reference spectra. The relation between these labels and the official version numbering of OMNO2A is described in Sect. S3 of the Supplement.

Solar spectrum

A high-resolution solar reference spectrum plays a key role in three aspects of the slant column processing, as it is used in: (a) the convolution of the high resolution trace gas references spectra (Sect. S2) and the generation of the H_2O_{vap} and Ring reference spectra (see below), (b) the wavelength calibration of the Earthshine radiance spectrum $I(\lambda)$, and (c) the interpolation of the wavelength grid of $I(\lambda)$ onto the wavelength grid of the Solar irradiance $I_0(\lambda)$ in Eq. (S2) in the Supplement.

[2]The full set of the OMI slit function – the slit functions for the 60 individual rows as well as the average slit function, both for the VIS (350–500 nm) and UV (310–380 nm) wavelength ranges – are available for download via the OMI website at http://www.knmi.nl/omi/research/product/

AMTD
7, 10619–10671, 2014

The high-resolution solar reference spectrum $I^h_{ref}(\lambda)$ used here is from Dobber et al. (2008). Figure 4 shows a comparison of the current (v2006) and updated (v2014) convolved solar reference spectra $I_{ref}(\lambda)$, where the difference between the two versions is due to the updated slit function. Differences between the two are 1.0–1.5 % at most wavelengths; near 430 nm, the difference is 2.1 %, while below 420 nm the differences is less than 1.0 %.

NO_2

The source for the NO_2 cross sections, the 220 K dataset of Vandaele et al. (1998), remains unchanged. Small differences between the current v2006 and the updated v2014 NO_2 reference spectra, seen in the top-left panel of Fig. 5, are related to the use of the updated slit function and $I^h_{ref}(\lambda)$ in the convolution given by Eq. (S12). These differences are of the order of 1–3 % and are therefore not expected to lead to significant changes in the retrieved NO_2 value.

O_3

The O_3 cross sections for the visible range in the current OMNO2A were based on the data from WMO (1975). These cross sections are replaced by the 223 K dataset from Bogumil et al. (2000), version 3.0 (December 2004), which is resampled using a cubic spline interpolation on a 0.01 nm grid and subsequently convolved with Eq. (S12). The top-right panel of Fig. 5 shows a comparison of the v2006 and v2014 O_3 reference spectra: for most wavelengths the difference is more or less an offset; at 420 nm the difference is about 35 %, at 450 nm about 10 %.

H_2O_{vap}

Absorption by water vapour (H_2O_{vap}) takes place in the form of a multitude of spectrally fine absorption lines, rather than as a smooth function of wavelength, so that

AMTD
7, 10619–10671, 2014

J. H. G. M. van Geffen et al.

convolution with Eq. (S12) cannot be simply applied to create a reference spectrum suitable for the DOAS retrieval. Instead, an effective reference spectrum for H_2O_{vap} absorption suitable for use in the DOAS fit is determined from two simulated reflectance spectra, one with and one without water vapour absorption – see Sect. S4 for details.

The bottom-left panel of Fig. 5 compares the updated v2014 H_2O_{vap} reference spectrum and the current v2006 one, which is based on Harder and Brault (1997) and was updated in 2007 based on HITRAN 2004 data. Some absorption peak values in the ranges 440–450 nm and 415–420 nm are clearly reduced, while the absorption in the range 425–430 nm is much weaker in the v2014 reference spectrum. Note also that some of the peaks in the v2006 seem to be narrower than the OMI slit function, indicating that something was clearly wrong with the v2006 H_2O_{vap} spectrum.

O_2–O_2

The collision between two oxygen molecules in the atmosphere gives rise to so-called O_2–O_2 absorption. The absorption peak around 446 nm lies in the NO_2 fit window, as does the tail of the absorption peak around 477 nm (cf. Fig. 3). The latter is used in the OMI OMCLDO2 data product for the retrieval of cloud information within the 460–490 nm wavelength window.

In the current OMNO2A processing, absorption by O_2–O_2 was not taken into account, as tests with v2006 pointed out that including O_2–O_2 did not significantly affect the RMS error of the fit. As described in Sect. 5.3, however, including O_2–O_2 improves the NO_2 fit in other ways.

Recently Thalman and Volkamer (2013) have released a new cross section database for O_2–O_2 absorption, given at 293 and 203 K, which compares very well with the data from Hermans et al. (1999) – which is used in many NO_2 retrievals, such as for the GOME-2 and SCIAMACHY data used above, and also for the OMCLDO2 cloud product – but has a higher signal-to-noise. For this reason the Thalman and Volkamer (2013) 293 K cross section data are selected as v2014 reference spectrum, but with a correction for a small spurious jump around 432 nm, for which the 203 K spectrum is

AMTD
7, 10619–10671, 2014

J. H. G. M. van Geffen et al.

used. Subsequently, the spectrum is resampled using a cubic spline interpolation on a 0.01 nm grid, followed by a convolution with Eq. (S12).

H_2O_{liq}

Accounting for absorption of light by liquid water (H_2O_{liq}), in particular in clear ocean water, has been considered before in the retrieval of glyoxal (Lerot et al., 2010) and of NO_2 (Richter et al., 2011). In the current OMNO2A processing H_2O_{liq} is not taken into account. As described in Sect. 5.3 including H_2O_{liq} clearly improves the spectral fit of NO_2 for clear-sky situations over clear ocean waters when using a fit window that is wider than 425–450 nm.

The absorption coefficients of liquid water are taken from Table 3 of Pope and Fry (1997). This reference spectrum is very smooth with wavelength, as can be seen in Fig. 3, so that a convolution of the spectrum is not strictly necessary. For consistency, however, convolution and I_0-correction are applied as with the other reference spectra. The absorption coefficients $\sigma_{H_2O_{liq}}$ have unit m^{-1}, so that the fit coefficient $N_{s,H_2O_{liq}}$ is the length of the average light path in water (in m).

Ring effect

Accounting for the Ring effect in the spectral fit requires either a Ring radiance spectrum $I_{ring}(\lambda)$ or a (pseudo) Ring differential cross section $\sigma_{ring}(\lambda)$, where the latter is essentially the difference between I_{ring} divided by a reference Sun spectrum and a low order polynomial.

For OMNO2A the $I_{ring}(\lambda)$ is computed following Chance and Spurr (1997), using the updated slit function, with the radiative transfer code DISAMAR (de Haan, 2011) in a line-by-line forward calculation on the basis of the high-resolution solar spectrum $I^h_{ref}(\lambda)$, assuming a pure Rayleigh atmosphere, i.e. without absorbing trace gases. The bottom-right panel of Fig. 5 shows the current v2006 and the updated v2014 Ring radiance reference spectra $I_{ring}(\lambda)$ for the nonlinear OMNO2A retrieval; differences are

AMTD
7, 10619–10671, 2014
Improved spectral fitting of nitrogen dioxide from OMI
J. H. G. M. van Geffen et al.

of the order of 2 %. The $\sigma_{ring}(\lambda)$ for the linear tests in Sect. S5 in the Supplement is constructed by subtracting a 2nd order polynomial from the ratio $I_{ring}(\lambda)/I_{ref}(\lambda)$.

4.2 Wavelength calibration

The measured solar irradiance spectrum $I_0(\lambda)$ used in the OMI NO_2 DOAS fit has been constructed from a yearly average of daily solar irradiance measurements by OMI during 2005 and has an accurate wavelength calibration.

From the start of the OMI mission, the level-1b radiance spectra $I(\lambda)$ of OMI are given on an initial assigned wavelength grid (Voors et al., 2006). This assigned wavelength grid – hereafter referred to as "wcA" – was at the time accurate enough for the NO_2 retrieval with OMNO2A. After the onset of the first row anomaly[3] in June 2007 and the subsequent growth of this issue after May 2008, however, the assigned wavelength grid appeared to be established less accurately and, consequently, hampered sufficiently accurate NO_2 retrievals in all rows, i.e. also in those not affected by the row anomaly.

The NO_2 fit results were improved by the introduction of a wavelength calibration in OMNO2A in January 2009. This wavelength calibration determines a wavelength shift from a fit against the reference solar spectrum $I_{ref}(\lambda)$, taking the Ring effect into account (cf. Voors et al., 2006), starting from the assigned wavelength grid wcA, independently for each ground pixel. The wavelength calibration in the current OMNO2A processing, called "wcB" hereafter, uses 408.0–423.0 nm as calibration window. This window, indicated by a horizontal line ending with open circles in Fig. 4, was chosen because it covers some distinct Fraunhofer features in the solar spectrum. Due to the nature of the OMI detector a squeezing or stretching of the wavelengths is unlikely, so the shift found from the calibration window is representative for the whole NO_2 fit window. The correspondence between the labels of the wavelength calibration and the official numbers of the OMNO2A processing is described in Sect. S3.

[3] See http://www.knmi.nl/omi/research/product/rowanomaly-background.php for an explanation and details.

AMTD
7, 10619–10671, 2014

4.2.1 Optimal calibration window

With the update of the solar reference spectrum $I_{ref}(\lambda)$ and the Ring radiance spectrum $I_{ring}(\lambda)$, discussed in Sect. 4.1, the wavelength shift determined in calibration window wcB changes quite a bit (see below). This change in the wavelength grid of the level-1b spectra directly improves the fit results: both the RMS and the error on the NO_2 SCD are reduced. Using the v2006 reference spectra for NO_2, O_3 and H_2O_{vap} (and not yet including O_2–O_2 and H_2O_{liq}), the changes due to the introduction of the new Solar and Ring reference spectra in the wcB wavelength calibration, averaged between 60° S and 60° N over the Pacific Ocean test orbit (see Sect. 5.1), are as follows:

- Wavelength shift: from +0.55 to -3.63×10^{-3} nm
- RMS error: from 1.39 to 1.15×10^{-4} (−17.4 %)
- NO_2 error: from 1.29 to 1.17×10^{15} molec cm^{-2} (−9.2 %)
- NO_2 SCD: from 8.54 to 8.04×10^{15} molec cm^{-2} (−5.8 %)

Since the spectral sampling of OMI (Sect. 2.1.1) is about 0.21 nm, a shift of -3.62×10^{-3} nm corresponds to 1.7 % of a wavelength pixel.

Given that the NO_2 fit results depend so clearly on the wavelength calibration, it was decided to test a range of calibration windows. Both the begin and end point of the calibration window where varied in steps of 0.5 nm, with a minimum size of 10 nm for the window, spanning the full NO_2 fit window 405–465 nm, a total of 5151 possible calibration windows. The fits where performed on the Pacific Ocean test orbit with all the new v2014 reference spectra, including O_2–O_2 and H_2O_{liq} absorption. From these calculations the "optimal calibration window", defined as the window with the lowest RMS and NO_2 error, was found to be 409.0–428.0 nm. This new calibration window, hereafter "wcN", is indicated in Fig. 4 by a horizontal line ending with filled circles. Clearly wcN covers one more distinct Fraunhofer line than wcB.

Discussion Paper | Discussion Paper | Discussion Paper | Discussion Paper |

AMTD

7, 10619–10671, 2014

Improved spectral fitting of nitrogen dioxide from OMI

J. H. G. M. van Geffen et al.

Title Page
Abstract Introduction
Conclusions References
Tables Figures
◀ ▶
Back Close
Full Screen / Esc
Printer-friendly Version
Interactive Discussion

Table 4 lists the calibration shift and the RMS and NO_2 error of the subsequent DOAS fit for calibration windows wcB and wcN. For comparison, Table 4 also gives the fit results using two other calibration windows: one spanning the full fit window ("wcF") and one more or less at the centre of the fit window ("wcC", indicated in Fig. 4 by a horizontal line ending with open triangles).

Some other orbits of the same day also show minimal RMS for the wcN window, while for some other orbits the minimum RMS is found in a slightly different window, but the difference between that RMS and the RMS of wcN is less than 0.05 %. Hence, wcN is selected as the optimal wavelength calibration window, to be implemented in the new version of the OMNO2A processor.

4.2.2 Uncertainty in NO_2 SCD related to calibration

The relationship between the RMS error of the fit and the resulting NO_2 SCD for the above mentioned 5151 possible calibration windows is shown in Fig. 6 for the Pacific Ocean test orbit. As expected, the relationship between the RMS error and the NO_2 SCD fit error (not shown) is linear, with a correlation coefficient of r = 0.998. There appears to be an almost perfect linear relationship between the NO_2 SCD and the shift of the calibration for the investigated range of wavelength shifts: NO_2 SCD [$\times 10^{15}$ molec cm^{-2}] = 2.325 × shift [$\times 10^{-2}$ nm] + 8.470, with a correlation coefficient of r = 0.99997. This linear relationship, applied to create the right axis in Fig. 6, implies that an error in the wavelength shift of 1×10^{-3} nm (0.5 % of a detector pixel) corresponds to a change in the NO_2 SCD of about 0.2×10^{15} molec cm^{-2}. Depending on the desired accuracy of the retrieved NO_2 column, e.g. for future satellite missions, the relationship poses firm requirements on the accuracy of the wavelength grid.

The minimum RMS is achieved for calibration window wcN (409.0–428.0). There are 112 possible calibration windows with an RMS within 0.5 % of the RMS of wcN and these calibration windows all have an end-wavelength below 430 nm. For these windows the NO_2 error ranges from 0.97 (the value for wcN) to 0.98×10^{15} molec cm^{-2}, and the NO_2 SCD ranges from 7.23 to 7.47×10^{15} molec cm^{-2}. The latter variation can

AMTD
7, 10619–10671, 2014

J. H. G. M. van Geffen et al.

be considered a measure for the uncertainty in the NO_2 SCD related to the wavelength calibration: 0.12×10^{15} molec cm^{-2} (0.05×10^{15} molec cm^{-2} in terms of the NO_2 VCD, when using a geometric air-mass factor).

5 Results of the OMI NO_2 retrieval improvements

The improvements for the OMNO2A NO_2 SCD retrieval discussed above comprise four steps:

1. the update of the high-resolution Solar reference spectrum and the Ring spectrum used for the wavelength calibration,
2. the change of the wavelength calibration window from wcB to wcN,
3. the update of the reference spectra of NO_2, O_3 and H_2O_{vap},
4. the inclusion of absorption by the O_2–O_2 collision complex and by liquid water.

The current OMNO2A processing system is referred to as number "v1" below, while the processing using the updated spectral fit settings is named "v2". The use of "v1" and "v2" is prompted by the fact that different version numbers apply to the current OMNO2A processing, as detailed in Sect. S3.

5.1 OMI data used for comparisons

For the comparison of the OMNO2A spectra fit results, the OMI orbit over the Pacific Ocean on 1 July 2005 (orbit number 05121, starting time 22:17 UTC, crossing the equator at about 140° W) is used. Other orbits of this day are used to evaluate the robustness of the findings. Only ground pixels with a solar zenith angle less than 75° are used; for most comparisons using orbit averages the data is limited to the latitude range [−60° : +60°]. Since stratospheric NO_2 is the main focus of this study, no filtering

AMTD
7, 10619–10671, 2014

of cloudy pixels is applied. The NO_2 retrievals are performed with the official processor, OMNO2A, in the fit window 405.0–465.0 nm with a 5th-degree polynomial.

5.2 Current vs. updated NO_2 SCD over the Pacific

Table 5 lists the NO_2 SCD, the NO_2 error and the RMS error values for the step-by-step improvements listed above. The first case in the table represents the current ("v1") OMNO2A settings for the SCDs used in the DOMINO v2.0 and NASA SP v2.1 NO_2 data products, case 2 represents the improved wavelength calibration, and case 4 the implementation of all updates together, i.e. the new "v2" version of OMNO2A.

Figure 7 shows the absolute values of (top row) and differences between (bottom row) cases 0, 2 and 4 in Table 5 of the RMS error (left column) and the NO_2 SCD (right column) for all 15 orbits. These results show that the wavelength calibration update (case 2) leads to large improvements in the spectral fitting of OMI NO_2 and the updates of the relevant reference spectra lead to smaller yet still significant improvements of the fit. The lower panels indicate that differences in RMS and NO_2 SCD vary only a little from orbit to orbit. Averaging the 15 orbit averages and giving changes w.r.t. the case-0 averages, the conclusions are that:

– the wavelength calibration updates reduce the RMS by 23 % and the SCD by 0.85×10^{15} molec cm^{-2},

– updates in the reference spectra further reduce the RMS by 9 % and the SCD by 0.35×10^{15} molec cm^{-2},

– in total the RMS improves by 31 % and the SCD is smaller, on average, by 1.20×10^{15} molec cm^{-2}.

The latitudinal dependency of the changes in the NO_2 SCD averaged over the 15 orbits is shown in Fig. 8. The change in NO_2 SCD resulting from the update of the wavelength calibration (blue line with squares) shows little variation with latitude, indicating that the imperfect wavelength calibration likely represents an additive offset of $0.85 \pm 0.04 \times 10^{15}$ molec cm^{-2} in the "v1 OMNO2A" retrieval.

On the other hand, the change in NO_2 SCD due to the update of the trace gas reference spectra and the inclusion of absorption by O_2–O_2 and H_2O_{liq} (black line with triangles in Fig. 8) depends clearly on latitude in absolute numbers and as a percentage of the NO_2 SCD: the change ranges from 0.1×10^{15} molec cm^{-2} (3 %) in the tropics to 0.8×10^{15} molec cm^{-2} (5 %) at high latitudes. That the change in the NO_2 SCD increases with latitude reflects the inclusion of O_2–O_2 absorption, which increases poleward, as indicated by the green short-dashed line in Fig. 8, due to the longer photon path.

Overall, the improved OMNO2A NO_2 SCD are reduced by 1.0–1.8×10^{15} molec cm^{-2} (10 to 16 %), the NO_2 SCD error by 0.2 to 0.3×10^{15} molec cm^{-2} (16 to 30 %), and the RMS error by 24 to 35 %, depending on latitude.

5.2.1 Evaluation with SCIAMACHY data

To facilitate a comparison of the improved spectral fit for OMI with data from SCIAMACHY, the NO_2 slant columns of both instruments are converted to vertical columns with the geometric air-mass factor M_{geo}, taking the curvature of the Earth's atmosphere into account (following Leue, 1999), which is important for $\theta_0 > 60°$:

$$M_{geo} = \frac{\sqrt{\cos^2\theta_0 + \delta^2 + 2\delta} - \cos\theta_0}{\delta} + \frac{1}{\cos\theta} \tag{2}$$

where $\delta \equiv h/r$ is the ratio between the height of the atmosphere h and the Earth radius r, θ_0 the solar zenith angle and θ the viewing zenith angle. This conversion ensures that the considerable differences in viewing angles between the two instruments do not affect the comparison.

Figure 9 shows a comparison of the OMI Pacific Ocean test orbit using the "v1 OMNO2A" and the "v2 OMNO2A" retrieval and of the SCIAMACHY data over the

Pacific Ocean of the same day (lines with symbols). Given SCIAMACHY's poor geographic coverage, the data of its three orbits over the Pacific are averaged for this comparison. The figure shows that the discrepancy between OMI and SCIAMACHY has been reduced from 1.2 to 0.8×10^{15} molec cm^{-2}.

The remaining offset between the new v2 OMNO2A and the SCIAMACHY NO_2 VCDs of 0.8×10^{15} molec cm^{-2} can be explained in part by the difference of about 0.5×10^{15} molec cm^{-2} expected due to the diurnal cycle of stratospheric NO_2. It should be kept in mind that SCIAMACHY has a negative bias of 0.1–0.2×10^{15} molec cm^{-2} w.r.t. GOME-2, as shown in Sect. 3.1 and by Hendrick et al. (2012), and w.r.t. an ensemble of stratospheric NO_2 limb sensor measurements as shown by Belmonte-Rivas et al. (2014). Secondly, the OMI NO_2 is retrieved by OMNO2A with a non-linear fit approach in the 405–465 nm window, while the SCIAMACHY NO_2 is retrieved by QDOAS with a linear fit approach in the 425–450 nm window (cf. Table 1). As mentioned in Sect. 5.4, the difference in fit window and fit approach explains another 0.1–0.2×10^{15} molec cm^{-2} in the difference between OMNO2A and SCIAMACHY.

5.3 About including O_2–O_2 and liquid water

The spectral residual of the NO_2 retrieval, defined by Eq. (S7) in the Supplement, describes the unexplained portion of the measured spectrum after a selected set of absorption signatures is accounted for in the fit model. Figure 10 shows the spectral residual of two cloud-free pixels along row 29 (0-based) of the Pacific Ocean test orbit: pixel 425 (top two curves, left axis) and pixel 592 (bottom two curves, right axis) using the updated reference spectra without (case 3 in Table 5, red solid lines) and with (case 4, blue dashed lines) taking absorption of O_2–O_2 and H_2O_{liq} into account. Pixel 425 (located at 20.2° S, 135.4° W) is over clear open ocean water with a low chlorophyll concentration[4] (0.028 mg m^{-3}), while pixel 592 (0.0° S,139.8° W) is over ocean water with a relatively high chlorophyll concentration (0.351 mg m^{-3}). An anti-correlation between the chlorophyll concentration and the liquid water absoprtion coefficient is expected, because the higher the chlorophyll concentration the more opaque the water is and therefore the shorter the penetration depth of light will be.

Figure 10 shows that the residual of pixel 425 has a clear structure in the range 445–465 nm in case liquid water absorption is not accounted for, while this structure does not appear for pixel 592. If H_2O_{liq} is included in the fit, the residual of pixel 425 is much reduced (by −35 %), while there is hardly any change in the residual of pixel 592 (by −2 %). For both pixels the NO_2 SCD reduces by about 6 % and the retrieved H_2O_{liq} fit coefficients are physically meaningful: for pixel 425 the H_2O_{liq} fit coefficient is 10.49 m, for pixel 592 it is 0.83 m.

Figure 11 shows the retrieved H_2O_{liq} coefficient (left axis, red solid line) as function of latitude for all ground pixels of row 29 for which a chlorophyll concentration is available. For comparison the graphs also shows the chlorophyll concentration and the cloud fraction for the same pixels; cloudiness clearly leads to lower H_2O_{liq} coefficients, as expected.

The inset of Fig. 11 shows the relationship between the H_2O_{liq} coefficient and the chlorophyll concentration. The graph makes a distinction between the ground pixels in the latitude range 40° S to 40° N (red croses) and outside that range (green circles). Pixels at latitudes above 40° N have chlorophyll concentration > 0.3 mg m^{-3} and for that reason low H_2O_{liq} coefficients. Pixels at latitudes below 40° S are measured at high solar zenith angle (above 70°), which apparently means low H_2O_{liq} coefficients (below about 2 m) even though chlorophyll concentrations are low (< 0.2 mg m^{-3}).

[4]Chlorophyll concentrations are extracted from NASA's Daily Assimilated Total Chlorophyll datasets with the Giovanni online data system from NASA GES DISC; data file: NOBM_DAtot.CR.data.01Jul2005.G3.output.txt

AMTD
7, 10619–10671, 2014

A world map of the H_2O_{liq} coefficient retrieved from all OMI orbits of 1 July 2005 is presented in Fig. 12. Open water areas are clearly visible on the map and land/sea boundaries show up sharply in some areas, such as the Mediterranean Sea, the Gulf of Mexico, around Madagascar, and the east coast of South America. Along the west coasts of South America, North America and Africa, for example, the H_2O_{liq} coefficient is very low, consistent with high chlorophyll concentrations there.

Including the absorption of H_2O_{liq} and the O_2–O_2 collision complex in the NO_2 fit is justified since their absorption is known to affect the radiance $I(\lambda)$ – unless including either of them would reduce the quality of the NO_2 fit, but that is not the case. When looking at the retrieved O_3 SCD, shown in the top-left panel of Fig. 13 as function of latitude, it is clear that without either of the two additional absorbers ozone values can be negative in the regions where absorption in open water is taking place. Adding both absorbers brings the retrieved O_3 SCD close to the values given in the official OMI ozone SCD data product OMDOAO3; the improvement is mostly due to including H_2O_{liq} absorption.

Including O_2–O_2 absorption but not H_2O_{liq} absorption does not result in realistic O_3 SCD values. If also H_2O_{liq} absorption is included, the retrieved O_2–O_2 SCD values appear realistic compared to the values given in the official OMI cloud data product OMCLDO2, which uses O_2–O_2 absorption around 475 nm. Including O_2–O_2 absorption has a small effect on the retrieved H_2O_{liq} coefficient (bottom-right panel in Fig. 13) and reduces the RMS error of the fit a little (not shown).

In summary: (a) including liquid water absorption leads to significant improvements in the NO_2 retrieval fit for pixels over clear open waters, without affecting other pixels, gives physically meaningful H_2O_{liq} and O_3 absorption coefficients, and (b) simultaneously including O_2–O_2 absorption gives realistic O_2–O_2 SCDs and improves the fit somewhat, notably at higher latitudes, where light paths are long.

AMTD
7, 10619–10671, 2014

5.4 Comparison between OMNO2A and QDOAS

The NO_2 spectral fits for SCIAMACHY and GOME-2 presented in this study have been performed with the QDOAS software in fit windows and with a fitting method different from OMNO2A (cf. Table 1). It is worthwhile to obtain an estimate of the sensitivity of the NO_2 SCD to the spectral fitting approach. Such estimates are important for satellite intercomparisons and the generation of long-term seamless multi-sensor data records. This preliminary comparison study, discussed in Sect. S5 of the Supplement, shows that the variability in the fit window and fit method selection introduces differences in the retrieved NO_2 SCD between -0.3 and $+0.6 \times 10^{15}$ molec cm^{-2} (i.e. up to 0.2×10^{15} molec cm^{-2} in terms of the NO_2 VCD).

5.5 Across track variation ("striping")

Due to instrumental effects OMI measurements show across-track biases, resulting from viewing zenith angle dependent calibration errors, which leads to so-called "stripes" in the retrieved NO_2 columns along the orbits (Boersma et al., 2011; Bucsela et al., 2013). In the above described comparisons no correction for the striping was applied; it was assumed that by taking averages over all rows of an orbit the striping effects average out. A comparison of along-track averages over latitudes ±45° (not shown) indicates that the striping neither improved nor worsened by the OMNO2A updates.

6 Concluding remarks

The OMI NO_2 slant column density (SCD) retrieval, OMNO2A, lies at the basis of the stratospheric and tropospheric NO_2 vertical column data products of OMI, notably the Dutch OMI NO_2 (DOMINO) and NASA Standard Product (SP) datasets. OMNO2A performs a DOAS spectral fit of NO_2 and a number of other trace gases in the fit window

AMTD
7, 10619–10671, 2014

405–465 nm, using a 5th-degree polynomial to represent the spectrally smooth part of the spectrum. This paper describes important updates for OMNO2A in order to improve the quality of the OMI NO_2 SCD data. The investigation was triggered by the finding that OMI stratospheric NO_2 columns are biased high w.r.t. other satellite sensors and ground-based measurements, which is caused by a bias in the underlying SCD data.

The improvements for the OMNO2A processor are:

- an update of the reference spectra of the trace gases included in the spectral fit,
- implementation of the wavelength and viewing angle dependency of the OMI slit function,
- optimisation of the wavelength calibration window based on minimising RMS and NO_2 errors,
- inclusion of absorption by O_2–O_2 and H_2O_{liq} to further reduce the RMS error.

Absorption by the O_2–O_2 collision complex increases with solar zenith angle due to increased light path length and is therefore important at higher latitudes, and the resulting O_2–O_2 SCDs have realistic values.

Accounting for absorption by liquid water (H_2O_{liq}) is particularly important for pixels over clear open waters with low chlorophyll concentrations and results in marked improvements to the spectral fit and assures that O_3 SCDs in the fit window have physically realistic values. Inclusion does not deteriorate the spectral fit for other, non-clear water, pixels. The values found for the H_2O_{liq} fit coefficient are physically meaningful for the areas where absorption in liquid water is relevant.

The updates of the wavelength calibration have the effect of removing an additive offset in the NO_2 SCD of 0.85×10^{15} molec cm^{-2} and reducing the RMS by about 23 % on average. The updates of trace gas reference spectra and the improved use of the OMI slit function for the convolution of these spectra lead to a reduction of the NO_2 SCD that depends on latitude, mainly related to the inclusion of O_2–O_2 absorption, varying from 0.2 to 0.6×10^{15} molec cm^{-2}, on average 0.35×10^{15} molec cm^{-2}; the RMS is reduced by about 9 % on average.

NO_2 SCD retrievals for other satellite and ground-based instruments employ different spectral fit windows and use different implementations of the DOAS technique, which leads to small differences in the resulting SCD values. A short investigation of this using the QDOAS software (Danckaert et al., 2012) shows that the uncertainty in NO_2 SCD related to the fit window and fit method may be as large as 0.3×10^{15} molec cm^{-2}.

The combination of improvements to the OMNO2A spectral fit lead to an overall reduction of the NO_2 SCD by about 1.2×10^{15} molec cm^{-2}, and a reduction of the NO_2 SCD error by 0.2–0.3×10^{15} molec cm^{-2} and of the RMS by 24–35 %. The reduction of the SCD appears to be to a large degree an additive offset, implying that the improvements in OMNO2A will probably affect stratospheric NO_2 most, and smaller effects may be expected on tropospheric NO_2.

Comparing the updated OMNO2A data with SCIAMACHY data over the Pacific Ocean shows that the discrepency between the two instruments is reduced from 1.2 to 0.8×10^{15} molec cm^{-2}. The remaining difference can be explained largely from the difference expected due to the diurnal cycle of stratospheric NO_2, which is higher by about 0.5×10^{15} molec cm^{-2} at 13:40 LT (when OMI measures) than at 09:30 (when SCIAMACHY measures), and the lower bias of SCIAMACHY relative to other instruments.

The updates to the OMNO2A retrieval systems seem, all in all, to be sufficient to remove the bias between the stratospheric NO_2 columns from OMI and those from other satellite and ground-based instruments. A final test of this requires the conversion of the retrieved SCD to the separate stratospheric and tropospheric NO_2 columns. This issue will be discussed in a forthcoming study that describes improvements to the data assimilation system of DOMINO, leading to a new DOMINO v3.0 dataset for the entire OMI period. The settings of the updated OMNO2A processing will be the initial configuration of the NO_2 retrieval for TROPOMI for reasons of consistency (van Geffen et al., 2014).

AMTD
7, 10619–10671, 2014

The Supplement related to this article is available online at doi:10.5194/amtd-7-10619-2014-supplement.

Acknowledgements. This work is funded by the Netherlands Space Office (NSO). The authors would like to thank Nickolay Krotkov, Sergey Marchenko, Andreas Richter and Pieter Valks for discussions and information on their approaches and studies. The authors would further like to thank Johan de Haan for discussions on and help with retrieval issues. Folkert Boersma acknowledges funding from NWO (Vidi Grant 864.09.001) and support by the EU-FP7 grant QA4ECV (607405). The research at BIRA-IASB (AGACC-II project) and the University of Liège (A3C and ACROSAT projects from the PRODEX program) has been financially supported by the Belgian Federal Science Policy Office (BELSPO), Brussels, and via the EU 7th Framework Programme project NORS (contract 284421). BIRA-IASB is thankful to M. P. Chipperfield (University of Leeds) for providing SLIMCAT data. The authors would also like to thank the International Foundation High Altitude Research Stations Jungfraujoch and Gornergrat (HFSJG, Bern).

References

Beirle, S., Boersma, K. F., Platt, U., Lawrence, M. G., and Wagner, T.: Megacity emissions and lifetimes of nitrogen oxides probed from space, Science, 333, 1737–1739, 2011. 10621

Belmonte-Rivas, M., Veefkind, P., Boersma, F., Levelt, P., Eskes, H., and Gille, J.: Intercomparison of daytime stratospheric NO_2 satellite retrievals and model simulations, Atmos. Meas. Tech., 7, 2203–2225, doi:10.5194/amt-7-2203-2014, 2014. 10622, 10628, 10629, 10641

Boersma, K. F., Bucsela, E., Brinksma, E., and Gleason, J. F.: OMI Algorithm Theoretical Basis Document – Vol. 4: OMI Trace Gas Algorithms, ATBD-OMI-02 Vers. 2.0, NASA Goddard Space Flight Cent., Greenbelt, Md., 13–28, 2002. 10624

Boersma, K. F., Eskes, H. J., and Brinksma, E. J.: Error analysis for tropospheric NO_2 retrieval from space, J. Geophys. Res., 109, D04311, doi:10.1029/2003JD003962, 2004. 10628

Boersma, K. F., Eskes, H. J., Dirksen, R. J., van der A, R. J., Veefkind, J. P., Stammes, P., Huijnen, V., Kleipool, Q. L., Sneep, M., Claas, J., Leitão, J., Richter, A., Zhou, Y., and Brunner, D.: An improved tropospheric NO_2 column retrieval algorithm for the Ozone Monitoring

AMTD
7, 10619–10671, 2014

Improved spectral fitting of nitrogen dioxide from OMI

J. H. G. M. van Geffen et al.

Instrument, Atmos. Meas. Tech., 4, 1905–1928, doi:10.5194/amt-4-1905-2011, 2011. 10624, 10628, 10644
Bogumil, K., Orphal, J., and Burrows, J. P.: Temperature dependent absorption cross sections of O_3, NO_2, and other atmospheric trace gases measured with the SCIAMACHY spectrometer, in Looking down to Earth in the New Millennium, Proceedings of the ERS-ENVISAT Symposium, 16–20 October 2000, Gothenburg, Sweden, ESA publication SP-461, 2000. 10632
Bovensmann, H., Burrows, J. P., Buchwitz, M., Frerick, J., Noel, S., Rozanov, V. V., Chance, K. V., and Goede, A. P. H.: SCIAMACHY: mission objectives and measurement modes, J. Atmos. Sci., 56, 127–150, 1999. 10622, 10624
Bucsela, E. J., Celarier, E. A., Wenig, M. O., Gleason, J. F., Veefkind, J. P., Boersma, K. F., and Brinksma, E. J.: Algorithm for NO_2 vertical column retrieval from the ozone monitoring instrument, IEEE T. Geosci. Remote, 44, 1245–1258, 2006. 10624
Bucsela, E. J., Krotkov, N. A., Celarier, E. A., Lamsal, L. N., Swartz, W. H., Bhartia, P. K., Boersma, K. F., Veefkind, J. P., Gleason, J. F., and Pickering, K. E.: A new stratospheric and tropospheric NO_2 retrieval algorithm for nadir-viewing satellite instruments: applications to OMI, Atmos. Meas. Tech., 6, 2607–2626, doi:10.5194/amt-6-2607-2013, 2013. 10624, 10644
Burrows, J. P., Weber, M., Buchwitz, M., Rozanov, V., Ladstätter-Weißenmayer, A., Richter, A., Debeek, R., Hoogen, R., Bramstedt, K., Eichmann, K.-U., Eisinger, M., and Perner, D.: The Global Ozone Monitoring Experiment (GOME): mission concept and first results, J. Atmos. Sci., 56, 151–175, 1999. 10622
Chance, K. V. and Spurr, R. J. D.: Ring effect studies: Rayleigh scattering, including molecular parameters for rotational Raman scattering, and the Fraunhofer spectrum, Appl. Optics, 36, 21, 5224–5230, 1997. 10622, 10634
Crutzen, P. J.: The influence of nitrogen oxides on the atmospheric ozone content, Q. J. Roy. Meteor. Soc., 96, 320–325, 1970. 10621
Danckaert, T., Fayt, C., and Van Roozendael, M.: QDOAS Software User Manual, Version 2.1, December 2012, BIRA-IASB, Brussels, Belgium, 2012. 10624, 10646
de Haan, J. F.: DISAMAR – Determining Instrument Specifications and Analyzing Methods for Atmospheric Retrieval – Algorithm description and background information, RP-TROPOMI-KNMI-066, issue 2.2.1, KNMI, the Netherlands, 2011. 10634

AMTD
7, 10619–10671, 2014

Improved spectral fitting of nitrogen dioxide from OMI

J. H. G. M. van Geffen et al.

Dirksen, R., Dobber, M. R., Voors, R., and Levelt, P.: Pre-launch characterization of the ozone monitoring instrument transfer function in the spectral domain, Appl. Optics, 45, 17, 3972–3981, 2006. 10631
Dirksen, R. J., Boersma, K. F., Eskes, H. J., Ionov, D. V., Bucsela, E. J., Levelt, P. F., and Kelder, H. M.: Evaluation of stratospheric NO_2 retrieved from the ozone monitoring instrument: intercomparison, diurnal cycle, and trending, J. Geophys. Res. 116, D08305, doi:10.1029/2010JD014943, 2011. 10622, 10624, 10629
Dobber, M., Voors, R., Dirksen, R., Kleipool, Q., and Levelt, P.: The high-resolution solar reference spectrum between 250 and 550 nm and its application to measurements with the ozone monitoring instrument, Sol. Phys., 249, 281–291, 2008. 10632
Fuglestvedt, J. S., Berntsen, T., Isaksen, I. S. A., Mao, H., Liang, X.-Z., and Wang, W.-C.: Climatic forcing of nitrogen oxides through changes in tropospheric ozone and methane, Atmos. Environ., 33, 961–977, 1999. 10621
Grainger, J. F. and Ring, J.: Anomalous Fraunhofer line profiles, Nature, 193, 762, doi:10.1038/193762a0, 1962. 10622
Harder, J. W. and Brault, J. W.: Atmospheric measurements of water vapor in the 442-nm region, J. Geophys. Res., 102, 6245–6252, 1997. 10633
Hendrick, F., Barret, B., Van Roozendael, M., Boesch, H., Butz, A., De Mazière, M., Goutail, F., Hermans, C., Lambert, J.-C., Pfeilsticker, K., and Pommereau, J.-P.: Retrieval of nitrogen dioxide stratospheric profiles from ground-based zenith-sky UV-visible observations: validation of the technique through correlative comparisons, Atmos. Chem. Phys., 4, 2091–2106, doi:10.5194/acp-4-2091-2004, 2004. 10627, 10629
Hendrick, F., Mahieu, E., Bodeker, G. E., Boersma, K. F., Chipperfield, M. P., De Mazière, M., De Smedt, I., Demoulin, P., Fayt, C., Hermans, C., Kreher, K., Lejeune, B., Pinardi, G., Servais, C., Stübi, R., van der A, R., Vernier, J.-P., and Van Roozendael, M.: Analysis of stratospheric NO_2 trends above Jungfraujoch using ground-based UV-visible, FTIR, and satellite nadir observations, Atmos. Chem. Phys., 12, 8851–8864, doi:10.5194/acp-12-8851-2012, 2012. 10621, 10626, 10627, 10628, 10629, 10641
Hermans, C., Vandaele, A. C., Carleer, M., Fally, S., Colin, R., Jenouvrier, A., Coquart, B., and Mérienne, M.-F.: Absorption cross-sections of atmospheric constituents: NO_2, O_2, and H_2O, Environ. Sci. Pollut. R., 6, 151–158, 1999. 10633
Jacob, D. J.: Introduction to Atmospheric Chemistry, Princeton University Press, Princeton, USA, 1999. 10621

AMTD
7, 10619–10671, 2014

Improved spectral fitting of nitrogen dioxide from OMI

J. H. G. M. van Geffen et al.

Krotkov, N. A., Bucsela, E. J., Celarier, E. A., Lamsal, L. N., and Swartz, W. H.: Improved OMI NO_2 Standard Product: Algorithm, evaluation, and results, EOS Aura Science Team Meeting, Pasadena, California, USA, 1–3 October, 2012. 10622

Lambert, J.-C., Granville, J., Van Roozendael, M., Sarkissian, A., Goutail, F., Müller, J.-F., Pommereau, J.-P., and Russell III, J. M.: A climatology of NO_2 profile for improved Air Mass Factors for ground-based vertical column measurements, in: Stratospheric Ozone 1999, edited by: Harris, N. R. P., Guirlet, M., and Amanatidis, G. T., Air Pollution Research Report 73 (CEC DG XII), 703–706, 1999. 10627

Lambert, J.-C., Granville, J., Van Roozendael, M., Müller, J.-F., Goutail, F., Pommereau, J.-P., Sarkissian, A., Johnston, P. V., and Russell III, J. M.: Global behaviour of atmospheric NO_2 as derived from the integrated use of satellite, ground-based network and balloon observations, Atmospheric Ozone – 19th Quad. Ozone Symp., Sapporo, Japan, 2000, edited by: NASDA, 201–202, 2000. 10627

Lerot, C., Van Roozendael, M., van Geffen, J., van Gent, J., Fayt, C., Spurr, R., Lichtenberg, G., and von Bargen, A.: Six years of total ozone column measurements from SCIAMACHY nadir observations, Atmos. Meas. Tech., 2, 87–98, doi:10.5194/amt-2-87-2009, 2009. 10625

Lerot, C., Stavrakou, T., De Smedt, I., Müller, J.-F., and Van Roozendael, M.: Glyoxal vertical columns from GOME-2 backscattered light measurements and comparisons with a global model, Atmos. Chem. Phys., 10, 12059–12072, doi:10.5194/acp-10-12059-2010, 2010. 10622, 10623, 10634

Leue, C.: Detektion der troposphärischen NO_2 Daten anhand von GOME, Ph.D. thesis, Univ. Heidelberg, Heidelberg, Germany, 1999. 10640

Levelt, P. F., van den Oord, G. H. J., Dobber, M. R. Dobber, Mälkki, A., Visser, H., de Vries, J., Stammes, P., Lundell, J. O. V., and Saari, H.: The ozone monitoring instrument, IEEE T. Geosci. Remote, 44, 1093–1101, 2006. 10622, 10623

Munro, R., Eisinger, M., Anderson, C., Callies, J., Corpaccioli, E. Lang, R., Lefebvre, A., Livschitz, Y., and Albinana, A. P.: GOME-2 on MetOp, ESA Publication SP 628, Paris, 2006. 10622, 10623

Murphy, D. M., Fahey, D. W., Proffitt, M. H., Liu, S. C., Chan, K. R., Eubank, C. S., Kawa, S. R., and Kelly, K. K.: Reactive nitrogen and its correlation with ozone in the lower stratosphere and upper troposphere, J. Geophys. Res., 98, 8751–8773, 1993. 10622

Platt, U.: Differential Optical Absorption Spectroscopy (DOAS), air monitoring by spectroscopic techniques, Chem. Anal., 127, 27–76, 1995. 10624

AMTD

7, 10619–10671, 2014

Platt, U. and Stutz, Z.: Differential Optical Absorption Spectroscopy, Principles and Applications, Springer, Heidelberg, Germany, 597 pp., 2008. 10624

Platt, U., Marquard, L., Wagner, T., and Perner, D.: Corrections for zenith scatterd light DOAS, Geophys. Res. Lett., 24, 1759–1762, 1997.

Pommereau, J.-P. and Goutail, F.: O_3 and NO_2 ground-based measurements by visible spectrometry during arctic winter and spring 1988, Geophys. Res. Lett., 15, 891–894, 1988. 10627

Pope, R. M. and Fry, E. S.: Absorption spectrum (380–700 nm) of pure water. II. Integrating cavity measurements, Appl. Optics, 36, 8710–8723, 1997. 10634

Richter, A., Begoin, M., Hilboll, A., and Burrows, J. P.: An improved NO_2 retrieval for the GOME-2 satellite instrument, Atmos. Meas. Tech., 4, 1147–1159, doi:10.5194/amt-4-1147-2011, 2011. 10623, 10634

Rinsland, C. P., Jones, N. B., Connor, B. J., Logan, J. A., Pougatchev, N. S., Goldman, A., Murcray, F. J., Stephen, T. M., Pine, A. S., Zander, R., Mahieu, E., and Demoulin, P.: Northern and Southern Hemisphere ground-based measurements of tropospheric carbon monoxide and ethane, J. Geophys. Res. 103, 28197–28217, 1998. 10627

Rinsland, C. P., Weisenstein, D. K., Ko, M. K. W., Scott, C. J., Chiou, L. S., Mahieu, E., Zander, R., and Demoulin, P.: Post Mount Pinatubo eruption ground-based stratospheric column measurements of HNO_3, NO, and NO_2 and their comparison with model calculation, J. Geophys. Res., 108, 4437, doi:10.1029/2002JD002965, 2003. 10628

Roscoe, H. K., Van Roozendael, M., Fayt, C., du Piesanie, A., Abuhassan, N., Adams, C., Akrami, M., Cede, A., Chong, J., Clémer, K., Friess, U., Gil Ojeda, M., Goutail, F., Graves, R., Griesfeller, A., Grossmann, K., Hemerijckx, G., Hendrick, F., Herman, J., Hermans, C., Irie, H., Johnston, P. V., Kanaya, Y., Kreher, K., Leigh, R., Merlaud, A., Mount, G. H., Navarro, M., Oetjen, H., Pazmino, A., Perez-Camacho, M., Peters, E., Pinardi, G., Puentedura, O., Richter, A., Schönhardt, A., Shaiganfar, R., Spinei, E., Strong, K., Takashima, H., Vlemmix, T., Vrekoussis, M., Wagner, T., Wittrock, F., Yela, M., Yilmaz, S., Boersma, F., Hains, J., Kroon, M., Piters, A., and Kim, Y. J.: Intercomparison of slant column measurements of NO_2 and O_4 by MAX-DOAS and zenith-sky UV and visible spectrometers, Atmos. Meas. Tech., 3, 1629–1646, doi:10.5194/amt-3-1629-2010, 2010. 10628

Schaub, D., Brunner, D., Boersma, K. F., Keller, J., Folini, D., Buchmann, B., Berresheim, H., and Staehelin, J.: SCIAMACHY tropospheric NO_2 over Switzerland: estimates of NO_x lifetimes

AMTD
7, 10619–10671, 2014

and impact of the complex Alpine topography on the retrieval, Atmos. Chem. Phys., 7, 5971–5987, doi:10.5194/acp-7-5971-2007, 2007. 10621
Shindell, D. T., Faluvegi, G., Koch, D. M., Schmidt, G. A., Unger, N., and Bauer, S. E.: Improved attribution of climate Forcing to emissions, Science, 326, 716–718, 2009. 10621
Sillman, S., Logan, J. A., and Wofsy, S. C.: The sensitivity of ozone to nitrogen oxides and hydrocarbons in regional ozone episodes, J. Geophys. Res., 95, 1837–1851, 1990. 10621
Thalman, R. and Volkamer, R.: Temperature dependant absorption cross-sections of O_2–O_2 collision pairs between 340 and 630 nm at atmospherically relevant pressure Phys. Chem. Chem. Phys., 15, 15371–15381, 2013. 10633
van Geffen, J. H. G. M., Boersma, K. F., Eskes, H. J., Maasakkers, J. D., and Veefkind, J. P.: TROPOMI ATBD of the total and tropospheric NO_2 data products, Report S5P-KNMI-L2-0005-RP version 1.0.0, September 2014, KNMI, De Bilt, the Netherlands, 2014. 10646
Van Roozendael, M., De Mazière, M., and Simon, P. C.: Ground-based visible measurements at the Jungfraujoch station since 1990, J. Quant. Sprectosc. Ra., 52, 231–240, 1994. 10628
Van Roozendael, M., Loyola, D., Spurr, R., Balis, D., Lambert, J.-C., Livschitz, Y., Valks, P., Ruppert, T., Kenter, P., Fayt, C., and Zehner, C.: Ten years of GOME/ERS-2 total ozone data – the new GOME data processor (GDP) version 4: 1. Algorithm description, J. Geophys. Res. 111, D14311, doi:10.1029/2005JD006375, 2006. 10625
Vandaele, A. C., Hermans, C., Simon, P. C., Carleer, M., Colin, R., Fally, S., Mérienne, M. F., Jenouvrier, A., and Coquart, B.: Measurements of the NO2 absorption cross-section from 42000 cm^{-1} to 10000 cm^{-1} (238–1000 nm) at 220 K and 294 K, J. Quant. Spectrosc. Ra., 59, 171–184, 1998. 10632
Vandaele, A. C., Fayt, C., Hendrick, F., Hermans, C., Humbled, F., Van Roozendael, M., Gil, M., Navarro, M., Puentedura, O., Yela, M., Braathen, G., Stebel, K., Tørnkvist, K., Johnston, P., Kreher, K., Goutail, F., Mieville, A., Pommereau, J.-P., Khaikine, S., Richter, A., Oetjen, H., Wittrock, F., Bugarski, S., Frieß, U., Pfeilsticker, K., Sinreich, R., Wagner, T., Corlett, G., and Leigh, R.: An intercomparison campaign of ground-based UV-Visible measurements of NO_2, BrO, and OClO slant columns. Methods of analysis and results for NO_2, J. Geophys. Res., 110, D08305, doi:10.1029/2004JD005423, 2005. 10628
Veefkind, J. P., Aben, I., McMullan, K., Förster, H., de Vries, J., Otter, G., Claas, J., Eskes, H. J., de Haan, J. F., Kleipool, Q., van Weele, M., Hasekamp, O., Hoogeveen, R., Landgraf, J., Snel, R., Tol, P., Ingmann, P., Voors, R., Kruizinga, B., Vink, R., Visser, H., and Levelt, P. F.: TROPOMI on the ESA Sentinel-5 Precursor: a GMES mission for global observations of the

atmospheric composition for climate, air quality and ozone layer applications, Remote Sens. Environ., 120, 70–83, 2012. 10622
Voors, R., Dirksen, R., Dobber, M., and Levelt, P.: Method of calibration to correct for cloud-induced wavelength shifts in the Auro satellite's Ozone Monitoring Instrument, Appl. Optics, 45, 3652–3658, 2006. 10635
World Health Organisation: Health Aspects of Air Pollution with Particulate Matter, Ozone and Nitrogen Dioxide, World Health Organisation, Bonn, Germany, 98 pp., 2003. 10621
World Meteorological Organisation (WMO): WMO Anual Repport, Bass & Johnsten, 1975. 10632
Zander, R., Mahieu, E., Demoulin, P., Duchatelet, P., Roland, G., Servais, C., De Mazière, M., Reimann, S., and Rinsland, C. P.: Our changing atmosphere: Evidence based on long-term infrared solar observations at the Jungfraujoch since 1950, Sci. Total Environ., 391, 185–195, 2008. 10627

AMTD
7, 10619–10671, 2014

J. H. G. M. van Geffen et al.

Table 1. Main settings of the DOAS retrieval of NO_2 slant column densities of the data versions used in this paper for the three satellite instruments OMI, GOME-2 and SCIAMACHY, as well as the groundbased instrument SOAZ; for the FTIR instrument (Sect. 2.3) a very different retrieval method is used.

	OMI	GOME-2	SCIAMACHY	SAOZ
wavelength range [nm]	405–465	425–450	426.5–451.5	425–495
secondary trace gases	O_3, H_2O_{vap}	O_3, H_2O_{vap}, O_2–O_2	O_3, H_2O_{vap}, O_2–O_2	O_3, H_2O_{vap}, O_2–O_2
pseudo-absorbers	Ring	Ring	Ring	Ring
degree of polynomial	5	3	2	3
fitting method	non-linear	linear	linear	linear
offset fitted	no	yes	yes	yes
DOAS retrieval code	OMNO2A	QDOAS	QDOAS	QDOAS
retrieval responsible	KNMI	BIRA-IASB	BIRA-IASB	BIRA-IASB
data version used	DOMINO v2.0	TM4NO2A v2.1	TM4NO2A v2.0	–

AMTD
7, 10619–10671, 2014

Table 2. Average differences in stratospheric NO_2 columns over the Pacific Ocean area (60° S–60° N, 140–180° W) of 2007 of OMI, GOME-2 and SCIAMACHY, where the averages are computed from monthly latitudinally binned data. The relative difference (right column) is given as percentage of the column values of the second instrument in the difference (e.g. w.r.t. SCIA in the difference OMI – SCIA). (Data source: http://www.temis.nl/)

instruments	absolute values [$\times 10^{15}$ molec cm^{-2}]	relative difference [%]
OMI – SCIA	$+1.28 \pm 0.15$	$+80.1 \pm 9.6$
OMI – GOME-2	$+1.14 \pm 0.18$	$+65.6 \pm 10.3$
GOME-2 – SCIA	$+0.14 \pm 0.09$	$+8.7 \pm 5.8$

AMTD
7, 10619–10671, 2014

Table 3. Average differences and corresponding standard deviations between SAOZ and FTIR groundbased measurements of NO_2 at Jungfraujoch (46.5° N, 8.0° E) and satellite based measurements by OMI, GOME-2 and SCIAMACHY, given both for the full data period and for the data period common to the satellite instruments (2007–2012). The relative difference (right column) is given as percentage of the groundbased NO_2 column values.

instruments period	absolute difference [$\times 10^{15}$ molec cm^{-2}]	relative difference [%]
OMI – SAOZ		
2004–2012	+0.43 ± 0.28	+18.3 ± 12.8
2007–2012	+0.48 ± 0.25	+20.9 ± 12.4
GOME-2 – SAOZ		
2007–2012	+0.09 ± 0.21	+5.4 ± 11.2
SCIAMACHY – SAOZ		
2002–2012	−0.12 ± 0.25	−5.2 ± 11.2
2007–2012	−0.02 ± 0.23	−1.3 ± 11.4
OMI – FTIR		
2004–2012	+0.56 ± 0.22	+23.0 ± 11.0
2007–2012	+0.54 ± 0.21	+21.5 ± 9.6
GOME-2 – FTIR		
2007–2012	+0.12 ± 0.17	+6.6 ± 9.1
SCIAMACHY – FTIR		
2002–2012	+0.02 ± 0.20	+0.7 ± 9.1
2007–2012	−0.001 ± 0.20	−0.2 ± 8.9

AMTD
7, 10619–10671, 2014

Improved spectral fitting of nitrogen dioxide from OMI

J. H. G. M. van Geffen et al.

Table 4. Main results of the wavelength calibration and spectral fit, using the v2014 reference spectra and the Pacific Ocean test orbit, for the different wavelength calibration windows mentioned in Sect. 4.2.

name	calib. window begin [nm]	end [nm]	shift $\times 10^{-3}$ [nm]	RMS $\times 10^{-4}$ [–]	NO_2 error $\times 10^{15}$ [molec cm^{-2}]
wcB	408.0	423.0	−3.63	0.97	0.99
wcN	409.0	428.0	−4.68	0.95	0.97
wcC	425.5	443.0	−7.70	1.09	1.10
wcF	405.0	465.0	−6.83	1.02	1.04

AMTD
7, 10619–10671, 2014

Table 5. Results of the NO_2 SCD fit for the different steps of the updates of the OMNO2A processing for the Pacific Ocean orbit. Case 0 represents the current OMNO2A version "v1" and case 4 the updated version "v2" settings. Cases 1 through 4 follow the updates listed at the beginning of Sect. 5. The numbers between bracket are percentage changes w.r.t. case 0. The NO_2 SCD error is given in absolute value and as percentage of the NO_2 SCD column. The NO_2 VCD in the last column is determined from the SCD and the geometric air-mass factor.

case	Solar Ring	calib. window	NO_2, O_3 H_2O_{vap}	O_2–O_2 H_2O_{liq}	RMS error [–]	NO_2 SCD [molec cm^{-2}]	NO_2 SCD error [molec cm^{-2}]	NO_2 SCD error [%]	NO_2 VCD [molec cm^{-2}]
0	v2006	wcB	v2006	no	1.39×10^{-4}	8.54×10^{15}	1.29×10^{15}	15.1	3.10×10^{15}
1	v2014	wcB	v2006	no	1.15 (−17.4 %)	8.04 (−5.8 %)	1.17 (−9.2 %)	14.5	2.92 (−6.1 %)
2	v2014	wcN	v2006	no	1.13 (−18.7 %)	7.75 (−9.2 %)	1.16 (−10.1 %)	14.9	2.81 (−9.6 %)
3	v2014	wcN	v2014	no	1.06 (−23.6 %)	7.96 (−6.8 %)	1.09 (−15.2 %)	13.7	2.89 (−7.0 %)
4	v2014	wcN	v2014	yes	0.94 (−32.0 %)	7.38 (−13.5 %)	0.97 (−24.6 %)	13.1	2.68 (−13.7 %)

AMTD
7, 10619–10671, 2014

J. H. G. M. van Geffen et al.

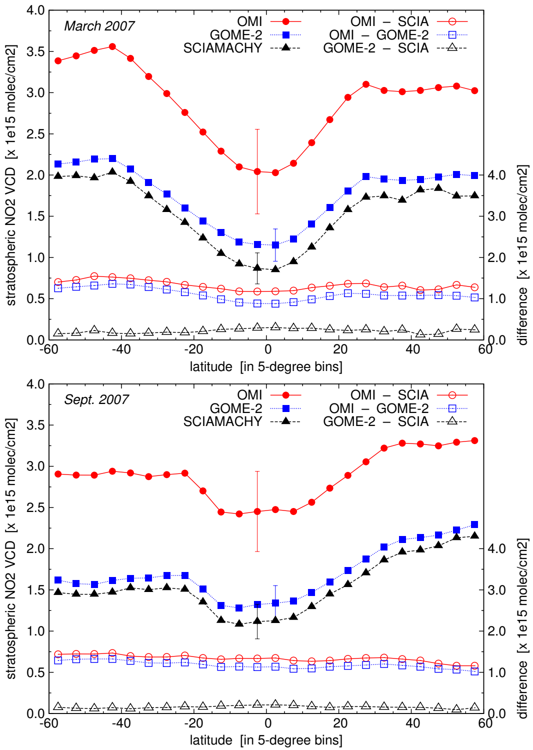

Figure 1. Monthly average stratospheric NO_2 VCD values (left axis; filled symbols) and absolute differences (right axis; open symbols) in 10^{15} molec cm^{-2} of OMI, GOME-2 and SCIAMACHY in March 2007 (top panel) and September 2007 (bottom panel) over the Pacific Ocean area (60° S–60° N, 140–180° W), as function of latitude. The error bars at the data points near the equator mark for that latitude bin the average of the standard deviation of the total VCD; see the text for details. Note that the VCD differences can also be read from the left axis by multiplying the left axis value by 2. (Data source: http://www.temis.nl/)

AMTD
7, 10619–10671, 2014

J. H. G. M. van Geffen et al.

Title Page
Abstract | Introduction
Conclusions | References
Tables | Figures
◀ | ▶
Back | Close
Full Screen / Esc
Printer-friendly Version
Interactive Discussion

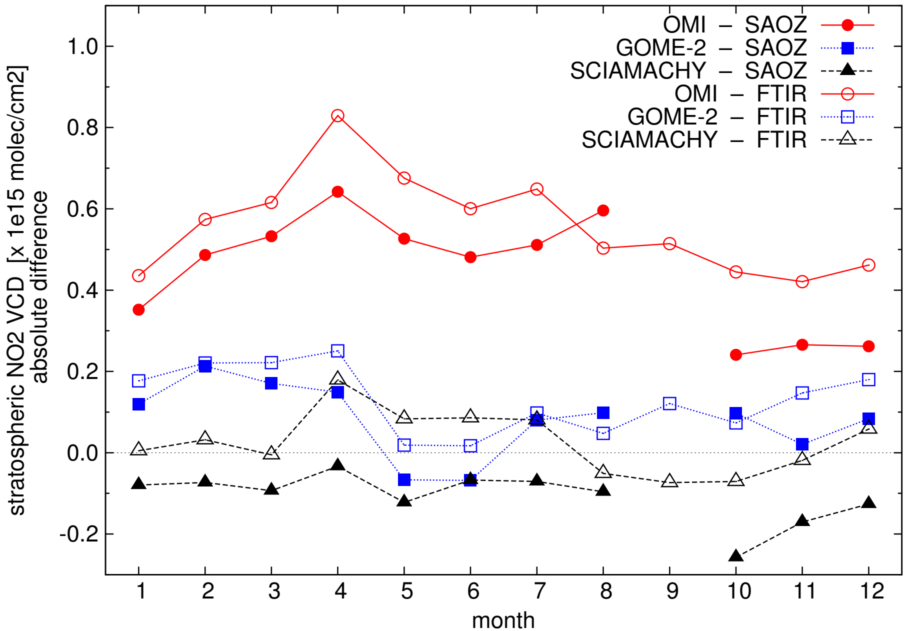

Figure 2. Monthly average absolute differences between SAOZ (filled symbols) and FTIR (open symbols) groundbased measurements of NO_2 in 10^{15} molec cm^{-2} at Jungfraujoch (46.5° N, 8.0° E) and satellite based measurements by OMI (2004–2012, red solid lines), GOME-2 (2007–2012, blue dotted lines) and SCIAMACHY (2002–2012, black dashed lines). There is insufficient SAOZ data in September for reliable averages.

AMTD
7, 10619–10671, 2014

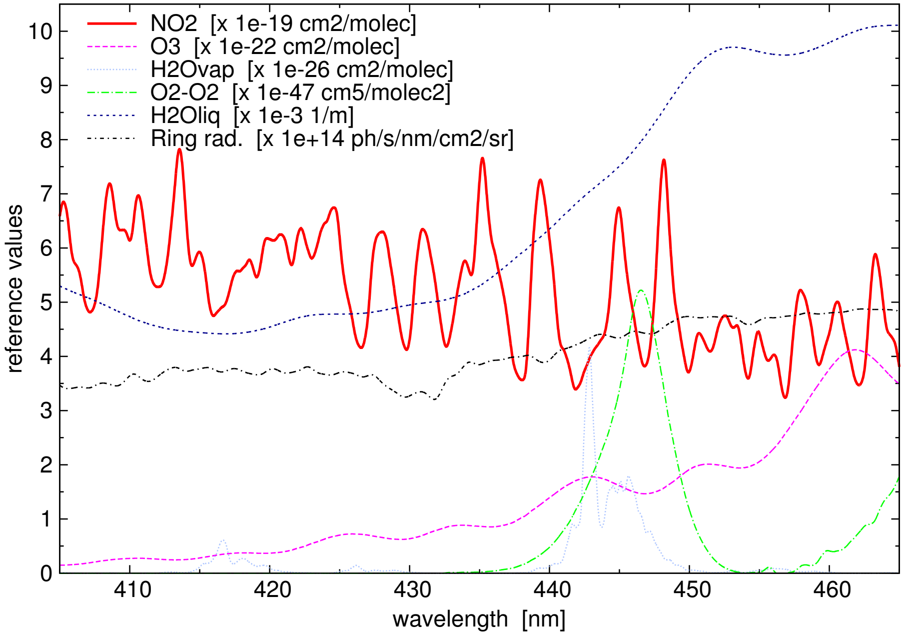

Figure 3. Graph of the absorption spectra of NO_2, O_3, H_2O_{vap}, O_2–O_2 and H_2O_{liq}, as well as the Ring radiance spectrum (I_{ring}) taken into account in the DOAS fit of the updated OMNO2A processor.

AMTD
7, 10619–10671, 2014

Improved spectral fitting of nitrogen dioxide from OMI

J. H. G. M. van Geffen et al.

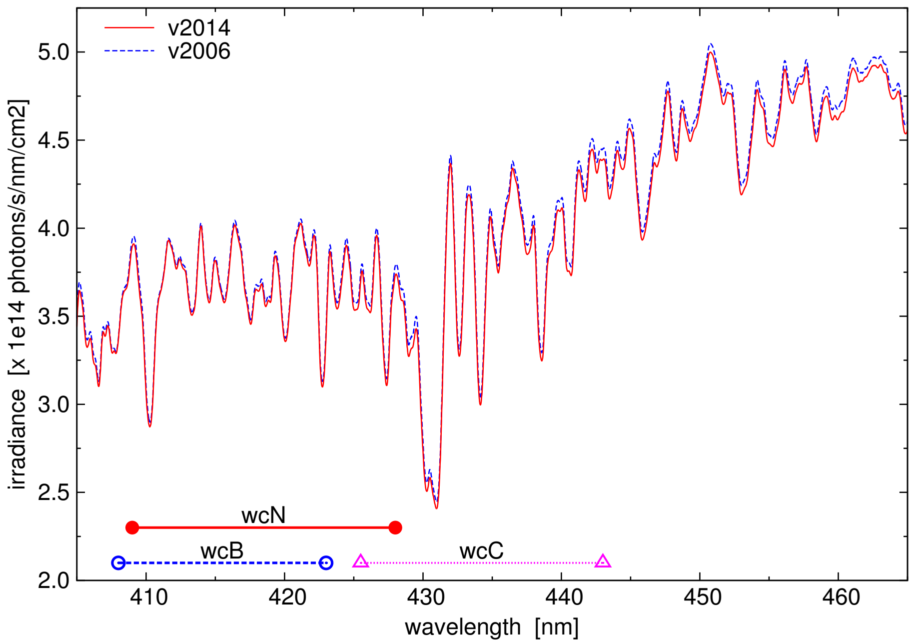

Figure 4. Comparison of updated v2014 (solid red line) and current v2006 (dashed blue line) convolved solar reference spectrum used in the wavelength calibration in OMNO2A. The two horizontal line pieces in the left bottom corner mark the old "wcB" (open circles) and new "wcN" (filled circles) window used for the wavelength calibration (Sect. 4.2); also shown is a test window "wcC" near the centre of the fit window.

AMTD
7, 10619–10671, 2014

J. H. G. M. van Geffen et al.

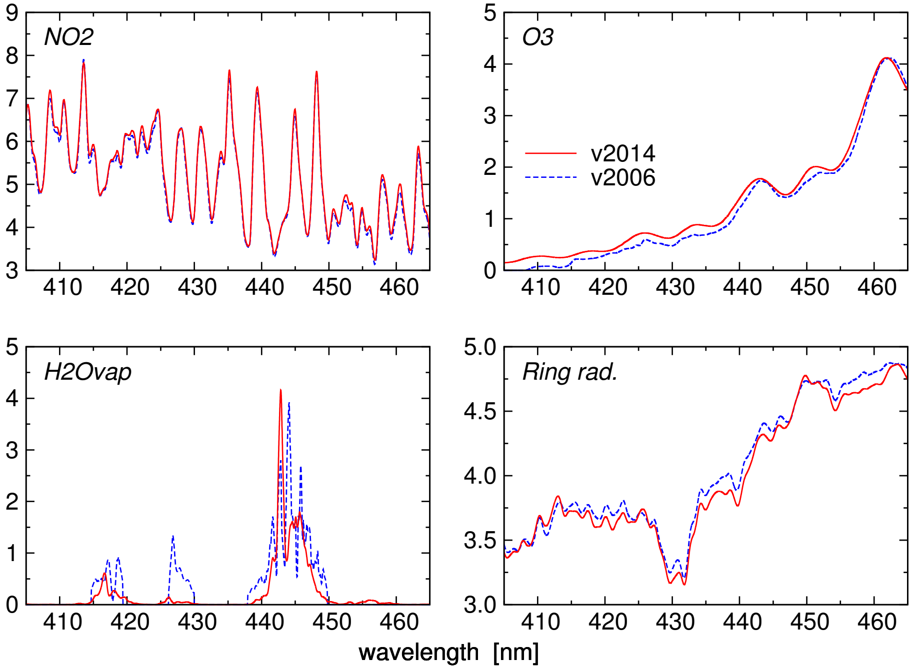

Figure 5. Comparison of updated v2014 (solid red lines; cf. Fig. 3) and current v2006 (dashed blue lines) references spectra of three trace gases and the Ring radiance spectrum in the OMNO2A processing, as discussed in Sect. 4.1. The units of the quantities are the same as in Fig. 3. Note that absorption by O_2–O_2 and H_2O_{liq} was previously not accounted for in OMNO2A.

AMTD
7, 10619–10671, 2014

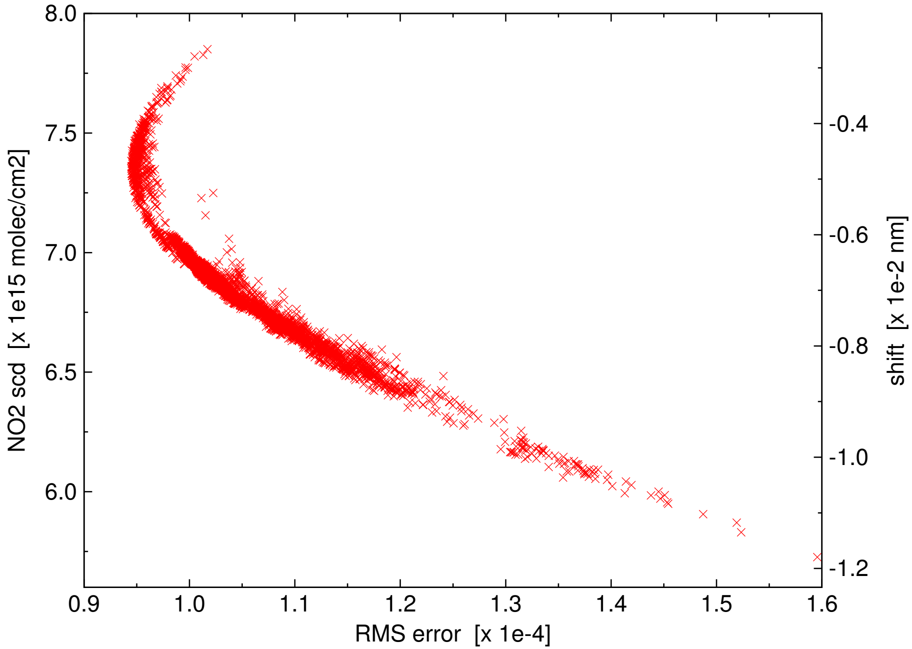

Figure 6. Relationship between the RMS error and the NO_2 SCD for the 5151 wavelength calibration windows investigated using the Pacific Ocean test orbit. The right axes of the main plot is approximate: it gives the shift of the wavelength calibration constructed from a linear relationship with the NO_2 SCD. See the text for more details.

AMTD
7, 10619–10671, 2014

J. H. G. M. van Geffen et al.

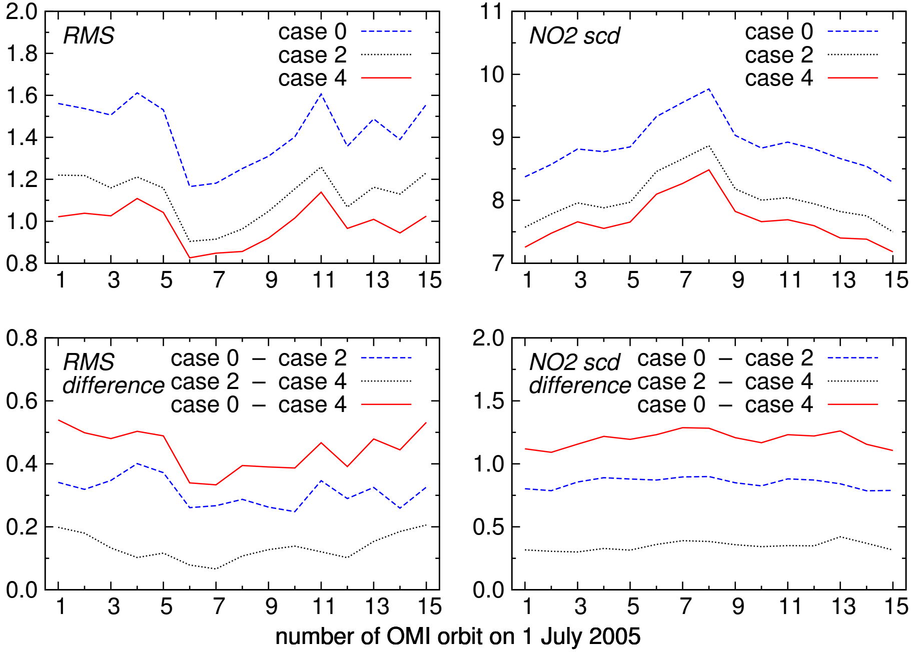

Figure 7. Absolute values (top row) and absolute differences (bottom row) of the orbit average RMS error (left column, $\times 10^{-4}$) and NO_2 SCD (right column, $\times 10^{15}$ molec cm^{-2}) as function of the OMI orbit number on 1 July 2005; the Pacific Ocean orbit is number 14. The case numbers refer to the cases listed in Table 5. The difference "case 0 – case 2" (blue line) refers to the updates of the wavelength calibration, "case 2 – case 4" (black line) to the updates of the reference spectra, and "case 0 – case 4" (red line) to all updates put together.

AMTD
7, 10619–10671, 2014

Improved spectral fitting of nitrogen dioxide from OMI

J. H. G. M. van Geffen et al.

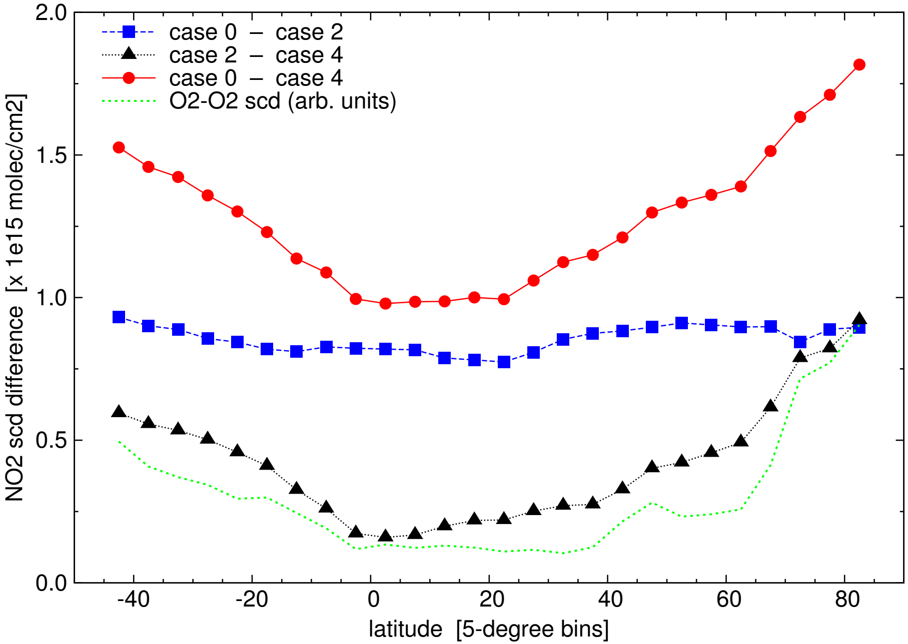

Figure 8. Absolute differences in the NO_2 SCD as function of latitude averaged over all 15 orbits. The case numbers refer to the cases listed in Table 5, similar to the bottom panels of Fig. 7. For comparison, the concentration of O_2–O_2 as function of latitude is shown in arbitrary units (green short-dashed line).

AMTD
7, 10619–10671, 2014

Improved spectral fitting of nitrogen dioxide from OMI

J. H. G. M. van Geffen et al.

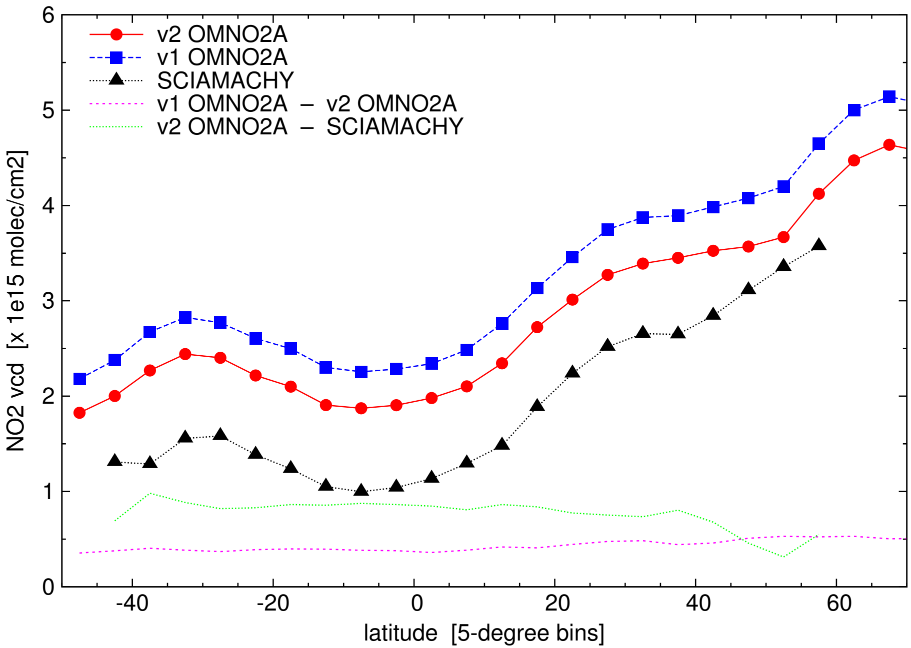

Figure 9. Comparison of the NO_2 VCD values (lines with symbols) of the new v2 OMNO2A (red circles) and old v1 OMNO2A (blue squares) retrieval for the Pacific Ocean orbit of 1 July 2005, and the average SCIAMACHY data (black triangles) over Pacific Ocean of the same day. The two lines without symbols show differences between the NO_2 VCD values. A numerical comparison between OMI and SCIAMACHY should be limited to latitudes below 45° because for higher latitudes the instrument cover different geographic areas. See the text for further details.

AMTD
7, 10619–10671, 2014

Improved spectral fitting of nitrogen dioxide from OMI

J. H. G. M. van Geffen et al.

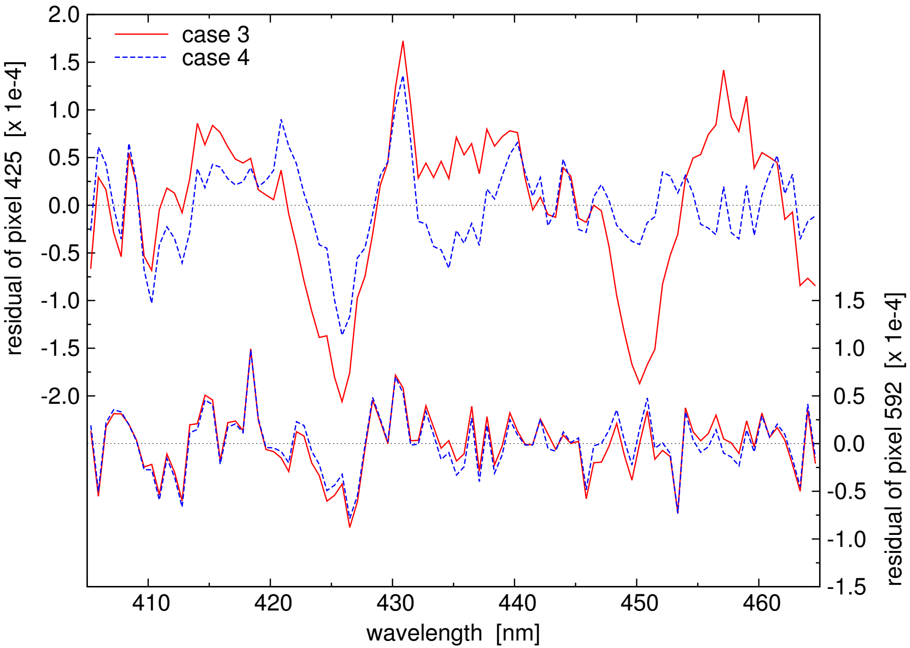

Figure 10. Spectral residual of the NO_2 retrieval fit with the updated reference spectra without (case 3, red solid lines) and with (case 4, blue dashed lines) O_2–O_2 and H_2O_{liq} absorption included for two detector pixels along row 29 (0-based): pixel 425 (top two curves, left axis) and pixel 592 (bottom two curves, right axis) of the Pacific Ocean test orbit; see the text for details on the pixel location. To clarify the graph, the wavelengths of three detector pixels are averaged, thus mimicing the fact that OMI's spectral resolution is about three times its spectral sampling.

AMTD
7, 10619–10671, 2014

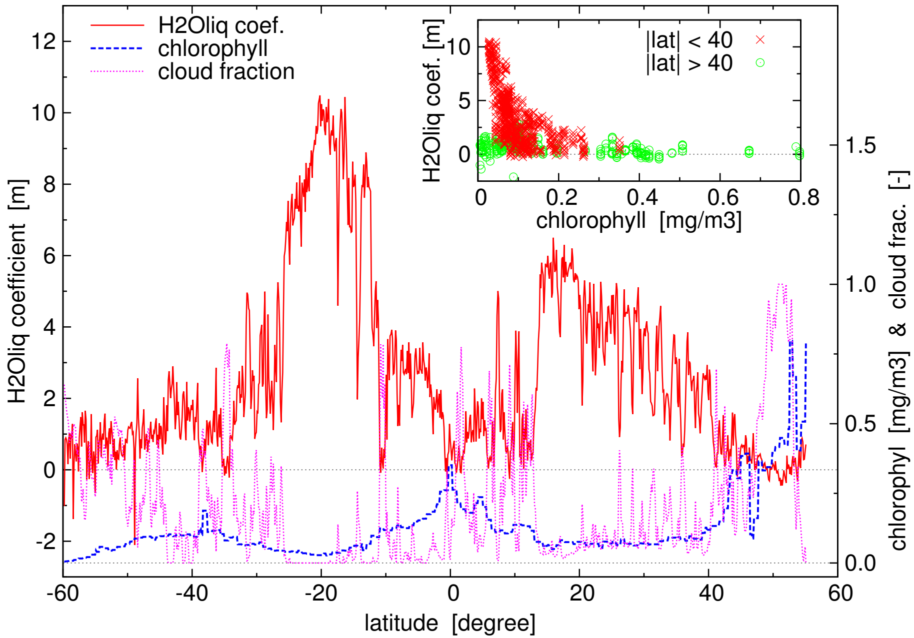

Figure 11. Retrieved H_2O_{liq} coefficient (in m; red solid line, left axis) as function of latitude for row 29 of the Pacific Ocean test orbit, showing only ground pixels for which chlorophyll concentration data is available. Also shown, with values along the right axis, are the chlorophyll concentration (in $mg\,m^{-3}$; blue dashed line) and the cloud cover fraction (magenta dotted line). The inset shows the H_2O_{liq} coefficient as function of the chlorophyll concentration separately for ground pixels with latitudes between ±40° (red crosses) and higer latitudes (green circles).

AMTD
7, 10619–10671, 2014

Improved spectral fitting of nitrogen dioxide from OMI

J. H. G. M. van Geffen et al.

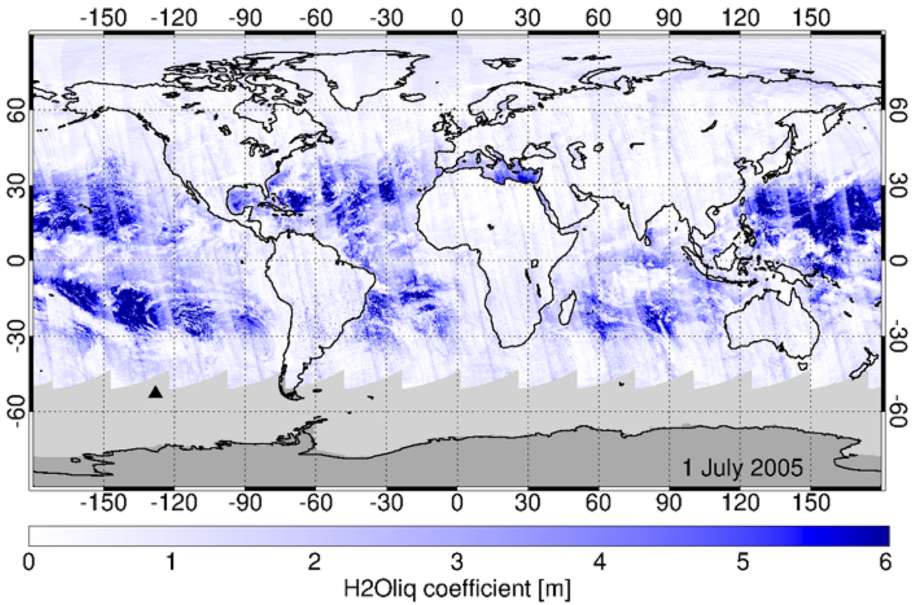

Figure 12. World map of the H_2O_{liq} coefficient (in m) based on all 15 OMI orbits of 1 July 2005; the Pacific Ocean test orbit is marked by a black triangle. All ground pixels with $\theta_0 < 75^\circ$ are plotted; no filtering for cloudy pixels was applied.

AMTD
7, 10619–10671, 2014

Improved spectral fitting of nitrogen dioxide from OMI

J. H. G. M. van Geffen et al.

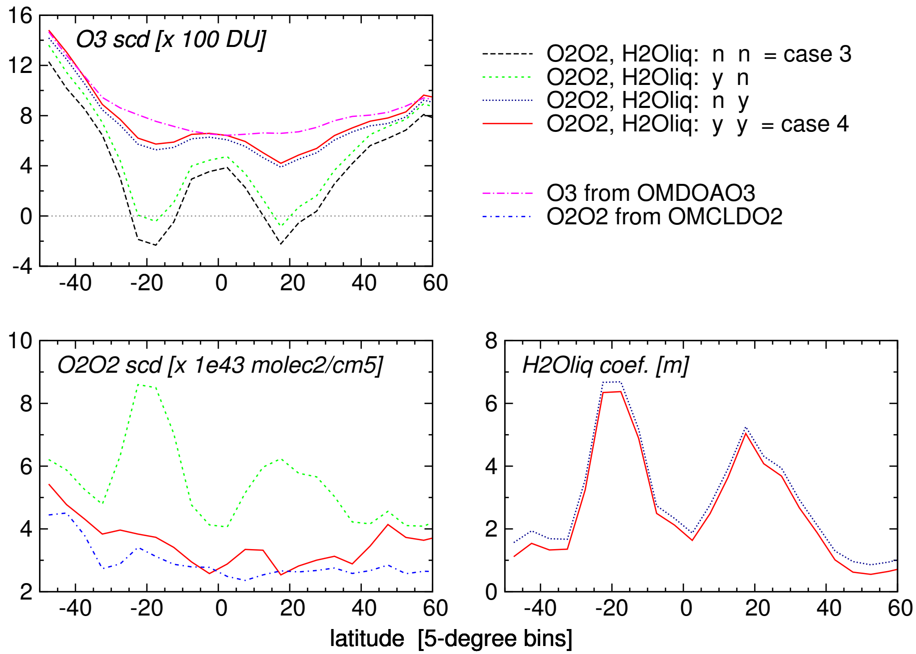

Figure 13. Retrieved values for the O_3 SCD (top-left), the O_2–O_2 SCD (bottom-left) and H_2O_{liq} coefficient (bottom-right) as function of latitude for the Pacific Ocean test orbit for retrievals without and with absorption by O_2–O_2 and H_2O_{liq} included in the fit as specified by the legend in the top-right corner; case numbers 3 (black dashed) and 4 (red solid) refer to the cases listed in Table 5. Also plotted are the O_3 SCD value from the OMI ozone slant column product OMDOAO3 (magenta long-dash-dotted) and the O_2–O_2 SCD value from the OMCLDO2 cloud product (blue short-dash-dotted).

AMTD
7, 10619–10671, 2014